Research Paper

Gold and antimony metallogenic relations and ore-forming process of Qinglong Sb(Au) deposit in Youjiang basin, SW China: Sulfide trace elements and sulfur isotopes

Jun Chen [a], Zhi-Long Huang [a,*], Rui-Dong Yang [b], Li-Juan Du [b,d], Ming-Yang Liao [c]

[a] State Key Laboratory of Ore Deposit Geochemistry, Institute of Geochemistry, Chinese Academy of Sciences, Guiyang, 550002, China
[b] College of Resources and Environmental Engineering, Guizhou University, Guiyang, 550025, China
[c] School of Mining Engineering, Guizhou Institute of Technology, Guiyang, 550003, China
[d] Key Laboratory of Karst Georesources and Environment, Ministry of Education, Guizhou University, Guiyang, 550025, China

ARTICLE INFO

ABSTRACT

In the northwestern margin of the Youjiang basin (NWYB) in SW China, many Carlin-like gold deposits are highly antimony (Sb)-rich, and many vein-type Sb deposits contain much Au. These deposits have similar ages, host rocks, ore-forming temperatures, ore-related alterations and ore mineral assemblages, but the Au and Sb metallogenic relations and their ore-forming process remain enigmatic. Here we investigate the large Qinglong Sb deposit in the NWYB, which has extensive sub-economic Au mineralization, and present a new metallogenic model based on in-situ trace elements (EPMA and LA-ICP-MS) and sulfur isotopes (NanoSIMS and fs-LA-MC-ICP-MS) of the ore sulfides. At Qinglong, economic Sb ores contain coarse-grained stibnite, jasperoid quartz and fluorite, whilst the sub-economic Au–Sb ores comprise dominantly veined quartz, arsenian pyrite and fine-grained stibnite. Three generations of ore-related pyrite (Py1, Py2 and Py3) and two generations of stibnite (Stb1 and Stb2) are identified based on their texture, chemistry, and sulfur isotopes. The pre-ore Py1 is characterized by the lower ore element (Au, As, Sb, Cu and Ag) contents (mostly below the LA-ICP-MS detection limit) and Co/Ni ratios (average 0.31) than the ore-stage pyrites (Py2 and Py3), implying a sedimentary/diagenetic origin. The Py2 and Py3 have elevated ore element abundance (maximum As = 6500 ppm, Au = 22 ppm, Sb = 6300 ppm, Cu = 951 ppm, Ag = 77 ppm) and Co/Ni ratios (average 1.84), and have positive As vs. Au–Sb–Cu–Ag correlations. Early-ore Stb1 has lower As (0.12–0.30 wt.%) than late-ore Stb2 (0.91–1.20 wt.%). These features show that the progressive As enrichment in ore sulfides is accompanied by increasing Au, Sb, Cu and Ag with the hydrothermal evolution, thereby making As a good proxy for Au. As-rich, As-poor and As-free zones are identified via NanoSIMS mapping of the Au-bearing pyrite. The As-rich zones in the Qinglong Au-bearing pyrites (Py2 and Py3) and ore stibnites (Stb1 and Stb2) have narrow δS_{H_2S} ranges (−8.9‰ to +4.1‰, average −3.1‰) and −2.9‰ to +6.9‰, average + 1.3‰), respectively, indicating that the Au-rich and Sb-rich fluids may have had the same sulfur source. Published in-situ sulfur isotopic data of pyrite As-rich zones from other Carlin-like Au deposits (Shuiyindong, Taipingdong, Nayang, Getang and Lianhuashan) in the NWYB have similar ore-fluid δS_{H_2S} values (−4.5‰ to +6.7‰, average −0.6‰) to those of Qinglong. Therefore, we infer that the sulfur of both Au and Sb mineralization was derived from the same magmatic-related source (0 ± 5‰) in the NWYB.

Moreover, the core of pyrites (Py1) has variable S isotope fractionation (−18.9‰ to +18.1‰, mostly +3‰ to +12‰), suggesting that the higher-^{34}S H_2S was produced by bacterial sulfate reduction (BSR). The hydrothermal pyrite (Py2 and Py3) $\delta^{34}S$ values gradually decrease with increasing As concentrations, and ultimately, within the restricted range (−5‰ to +5‰) in As-rich zones. This variation implies that the As-rich pyrite was formed through ongoing interactions of the magmatic-hydrothermal fluid with pre-existing sedimentary pyrites, causing the progressive decreasing $\delta^{34}S$ values with As content increase, Hence, the fluid/mineral interaction may have generated the observed variation in $\delta^{34}S$ and As contents. Overall, comparing the Au and Sb deposits in the NWYB, we favor a magmatic-related source for the Au–Sb–As-rich fluids, but the Au- and Sb-ore fluids were likely evolved at separate stages in the ore-forming system.

1. Introduction

Carlin-type deposits represent a major source of gold, and account for ~8% of the current global gold production (Muntean and Cline, 2018). Following the definition of the Carlin-type deposits in Nevada, similar ore deposits (Carlin-like) were reported in the Youjiang basin of SW China (e.g., Peters et al., 2007; Su et al., 2009a, 2018; Hu and Zhou, 2012; Hou et al., 2016; Xie et al., 2018a, Fig. 1A and B), which represents the world's second largest Carlin-type/-like Au province after Nevada with >800 tonnes (t) of gold (Wang et al., 2018). In the northwestern margin of the Youjiang basin (NWYB), abundant Carlin-like gold deposits (e.g., Shuiyindong, Nibao, Getang) and vein-type antimony (Sb) deposits (Qinglong) occur as clusters or belts (Wang et al., 2018), constituting a low-temperature metallogenic province in South China (Hu et al., 2017). A special feature of the NWYB is that the Carlin-like gold deposits are anomalously Sb-rich (Hu et al., 2002; Su et al., 2012; Xie et al., 2018a, b), whereas the vein-type Sb deposits also have sub-economic Au endowments. For instance, the large Qinglong deposit contains ca. 300 kt Sb resource (Guizhou BGMR, unpubl), and recent exploration discovered also extensive Au mineralization (0.1–9.9 g/t) (Chen et al., 2018). Meanwhile, the largest carbonate-hosted gold deposit in the region (Shuiyindong; resource: 263 t Au at 5 g/t) also contains sub-economic stibnite mineralization (Su et al., 2012; Xie et al., 2018b).

The Paleozoic–Mesozoic Youjiang basin lies in the southwestern Yangtze craton, and has experienced multistage deformation from the Late Devonian (ca. 364 Ma) to the Early Cretaceous (ca. 142 Ma). The deformation includes folding-thrusting and uplifting of the late Caledonian Orogeny, Devonian–Triassic extensional tectonics, late Indosinian (Triassic) foreland folding-thrusting, and the Yanshanian (Jurassic–Cretaceous)–Himalayan (latest Cretaceous–Eocene) uplifting and denudation (Guizhou BGMR, 1987). These tectonic events, especially the Yanshanian one (~140 Ma), have formed the complex basinal structures and widespread low-temperature Sb–Au–As–Hg mineralization (Su et al., 2009b; Chen et al., 2019; Zheng et al., 2019). The Au and Sb mineralization ages have been estimated by various methods, e.g., for the Nibao gold deposit, the quartz from fault-controlled and strata-bound orebodies yielded Rb–Sr isochron ages of 142 ± 3 Ma and 141 ± 2 Ma (Zheng et al., 2019), and the hydrothermal apatite yielded SIMS Th–Pb age of 141 ± 3 Ma (Chen et al., 2019). Meanwhile, hydrothermal calcite from the Zimudang gold deposit yielded Sm-Nd age of 148 ± 5 Ma (Wang, 2013),

whilst hydrothermal fluorite from the Qinglong Sb(Au) deposit yielded Sm-Nd ages of 142 Ma and 148 Ma (Peng et al., 2003). Based on these age data, the regional Sb mineralization was interpreted to have similar age and tectonic setting to its Carlin-like Au counterpart in the basin, which may imply a possible genetic link between the two. Although the gold deposits have been mined and studied for decades (e.g., Hu et al., 2002, 2017; Peters et al., 2007; Su et al., 2008, 2009a, b, 2012, 2018; Hu and Zhou, 2012; Chen et al., 2015; Tan et al., 2015; Hou et al., 2016; Pi et al., 2017; Zhu et al., 2017; Yan et al., 2018; Li et al., 2020b), publications on the Sb deposits are rare (Peng et al., 2003; Chen et al., 2018). Questions remain on the possible genetic link between the Au and Sb mineralization and their respective origin, answering which is crucial to the buildup of Au–Sb metallogenic model for the basin.

Previous studies have identified the incorporation of low-temperature ore-related elements (Au, As, Sb, Cu, Hg, and Tl) into sulfide minerals (e.g., pyrite, stibnite, realgar and orpiment) from the Youjiang basin (e.g., Peters et al., 2007; Hu and Zhou, 2012; Su et al., 2018). Based on sulfur isotope evidence, some authors suggested that the Au and Sb were derived from a sedimentary or diagenetic source (Chen et al., 1992; Qin and Liu, 2006), whereas some others called upon an epigenetic input from concealed felsic intrusions (Su et al., 2009b; Wang et al., 2013; Chen et al., 2018; Xie et al., 2018b). In addition, a sedimentary-igneous mixed source has also been proposed (Li et al., 2005; Xia, 2005; Wang et al., 2010; Hou et al., 2016). Previous scholars have determined that Au is transported as bisulfide complexes in acidic hydrothermal fluids and coprecipitates with pyrite and arsenopyrite (e.g., Seward, 1973; Hu RZ et al., 2002; Su et al., 2008, 2012; Chen et al., 2015; Hu et al., 2018a, b), and Sb is mainly transported as bisulfide ($Sb_2S_2(OH)_2^0$) complexes and/or hydroxybisulfide ($HSb_2S_4^-$) complexes (William Jones and Norman, 1997). High-precision sulfur trace-element and isotope data of auriferous pyrite and stibnite is therefore a key to understand the source(s) of sulfur, and probably also of Au and Sb.

In-situ analytical methods, such as laser ablation inductively coupled plasma-mass spectrometry (LA-ICP-MS) and secondary ion mass spectrometry (SIMS) have been used for high-precision sulfur trace-element and isotope composition measurements. In recent years, high-resolution (100-nm) NanoSIMS has been used to determine the concentrations/distributions of Au and other ore-related elements (detection limits down to ppb) and sulfur isotope ratios ($^{34}S/^{32}S$) in auriferous pyrite from Carlin-type/-like gold deposits (Barker et al., 2009; Zhang et al.,
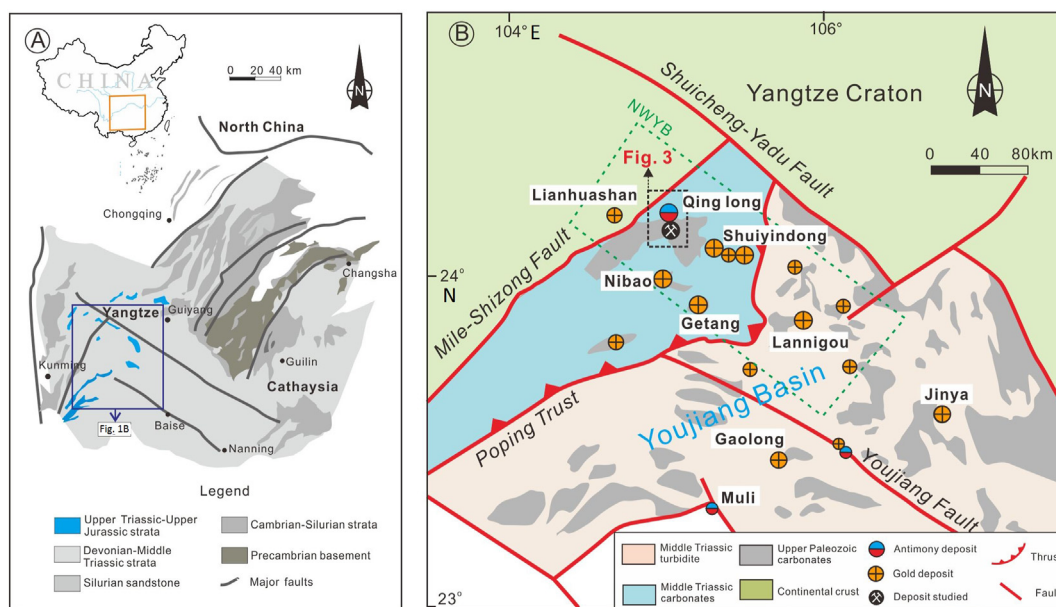

Fig. 1. (A) Location map of the Youjiang basin (modified after Hu et al., 2012). (B) Tectonic units and Au–Sb deposits in the Youjiang basin, SW China (modified after Chen et al., 2018).

2014; Yan et al., 2018).

In this study, high-resolution in-situ EPMA (electron probe micro-analysis), LA-ICP-MS, fs-LA-MC-ICP-MS and NanoSIMS mapping was conducted to reveal the spatial distribution of trace elements (e.g., Au, As, S, Cu and Sb) and S-isotopes in the auriferous pyrite and stibnite from Qinglong. Published in-situ SHRIMP/LA-MC-ICP-MS sulfur isotope data of other gold deposits in the NWYB (e.g., Shuiyindong, Getang, Lianhuashan, Taipingdong and Nayang; Fig. 1B) were also compiled to identify possible source(s) of the Au and Sb ore fluids. We then propose a new model to illustrate the genetic relations between Au and Sb mineralization in the region.

2. Geological background

2.1. Youjiang basin

The Youjiang basin is divided by the Poping thrust into two sedimentary successions (Fig. 1B). To the northwest of the thrust, a shallow-water Permian platform carbonate sequence is interbedded with calcareous siltstone-sandstone and the Permian Emeishan flood basalt; whereas to the southeast a Triassic terrigenous clastic succession is present (Su et al., 2018). The Permian platform carbonate or calcareous/carbonaceous rocks hosts several stratabound deposits, e.g., the Shuiyindong, Getang, Nibao Au deposits and Qinglong Sb(Au) deposit. It is interpreted that these deposits were formed in a tectonic setting similar to the Carlin-type deposits in Nevada, i.e., passive-margin sediment deposition in a rifted cratonic margin (Xie et al., 2018b), and then deformed by later orogenic events (Cline et al., 2013).

Magmatism in the Youjiang basin is represented by the Late Permian dolerite intrusions (zircon U–Pb age: ~259 Ma; Zhang and Xiao, 2014), quartz porphyry dykes (zircon U–Pb age: 140–130 Ma; Zhu et al., 2016)

and lamprophyre dykes (zircon U–Pb age: 88–85 Ma; Liu et al., 2010) (Fig. 2). Although a wide age range (various dating methods: 275–46 Ma) has been reported for the Au–Sb mineralization in the basin (e.g., Hu et al., 2002; Su et al., 2009b; Chen et al., 2015; Pi et al., 2017; Chen et al., 2019; Zheng et al., 2019), these ages are mainly clustered around the Late Triassic (235–200 Ma; Chen et al., 2015; Pi et al., 2017) and Late Jurassic to Early Cretaceous (148–134 Ma; Peng et al., 2003; Su et al., 2009b; Chen et al., 2019; Zheng et al., 2019). New age data from integrated *in-situ* zircon geochronology of mineralized tuffs from the Carlin-like Au deposits in Youjiang basin also indicate that the gold mineralization occurred at 239 Ma and 129–136 Ma (Zhu et al., 2020). It is noteworthy that felsic dykes are present in some of the Youjiang Carlin-like Au deposits, with intrusive ages (zircon U–Pb age: 140–130 Ma, Zhu et al., 2016) broadly coeval to the regional Au–Sb mineralization. In addition, aeromagnetic surveys revealed deep-seated plutons in the Youjiang basin (Wang et al., 2009, 2015; Fig. 2).

2.2. Qinglong Sb (Au) deposit

The large Qinglong Sb (Au) deposit in the NWYB has eight ore blocks (i.e., Dachang, Shuijingwan, Dishuiyan, Gulu, Houpo, Xishe, Sanwangping and Heishanjing), and several lateritic Au (e.g., Laowanchang) and fluorite deposits are discovered near Qinglong (Fig. 3). Local stratigraphy includes the Middle Permian Maokou Formation (Fm.), Middle Permian "Dachang layer", Upper Permian Emeishan flood basalt and the Longtan Fm. The Middle Permian Maokou Fm. Is dominated by thick-bedded limestone (Fig. 4A). The Dachang layer, the main ore host at Qinglong, overlies the Maokou Fm (Fig. 4A–D). and is divided into the lower, middle and upper units. The lower unit consists of siliceous rock, mudstone and silicified limestone (Chen et al., 2018). The middle unit is dominated by brecciated basalt, tuff and silicified limestone with
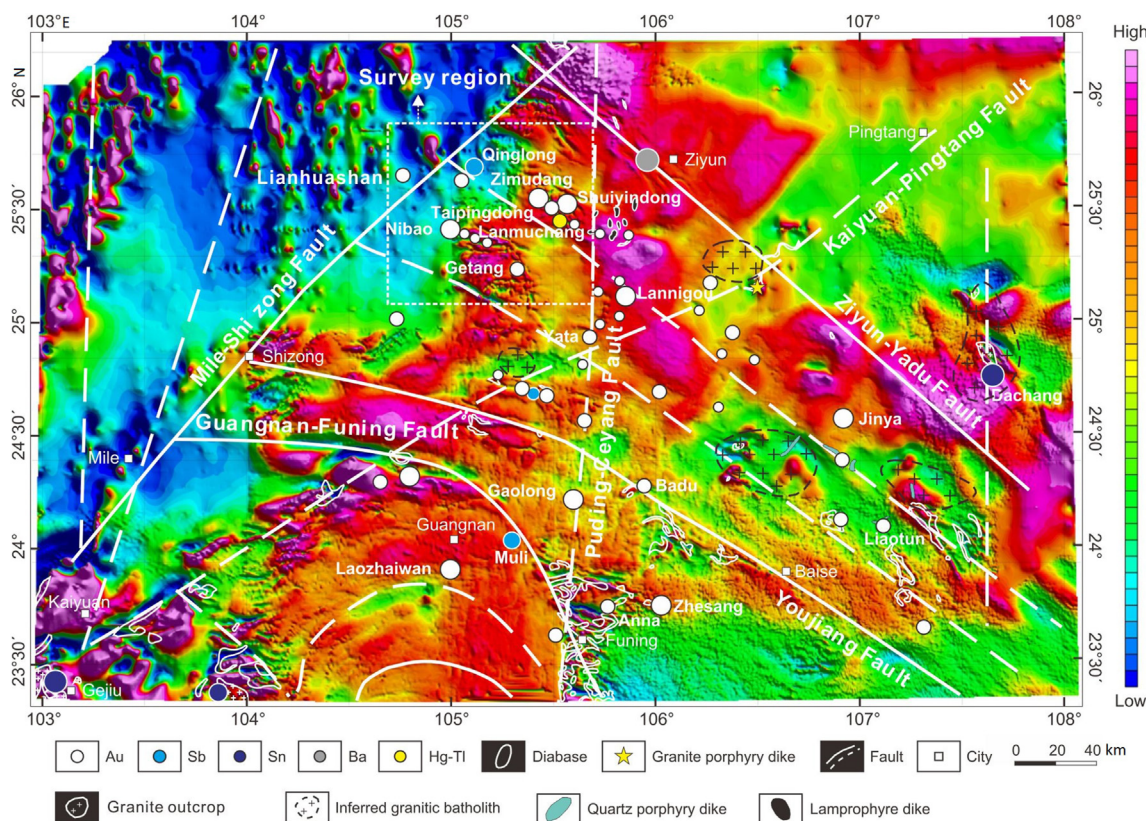

Fig. 2. Total aeromagnetic intensity map of the Youjiang basin, showing the distributions of major mafic-felsic intrusions, faults, and ore deposits (Au, Sb, Pb–Zn, Sn-polymetallic, barite) in the Youjiang basin. Most magnetic highs correspond to the distribution of Emeishan flood basalt, diabase intrusions, and lamprophyre dikes. Deep granitic batholiths are inferred from regional Bouguer gravity anomalies (black dashed circles), which are likely co-magmatic with the porphyry dikes (yellow star) and quartz porphyry dike outcrops. Figure modified from Su et al. (2018).
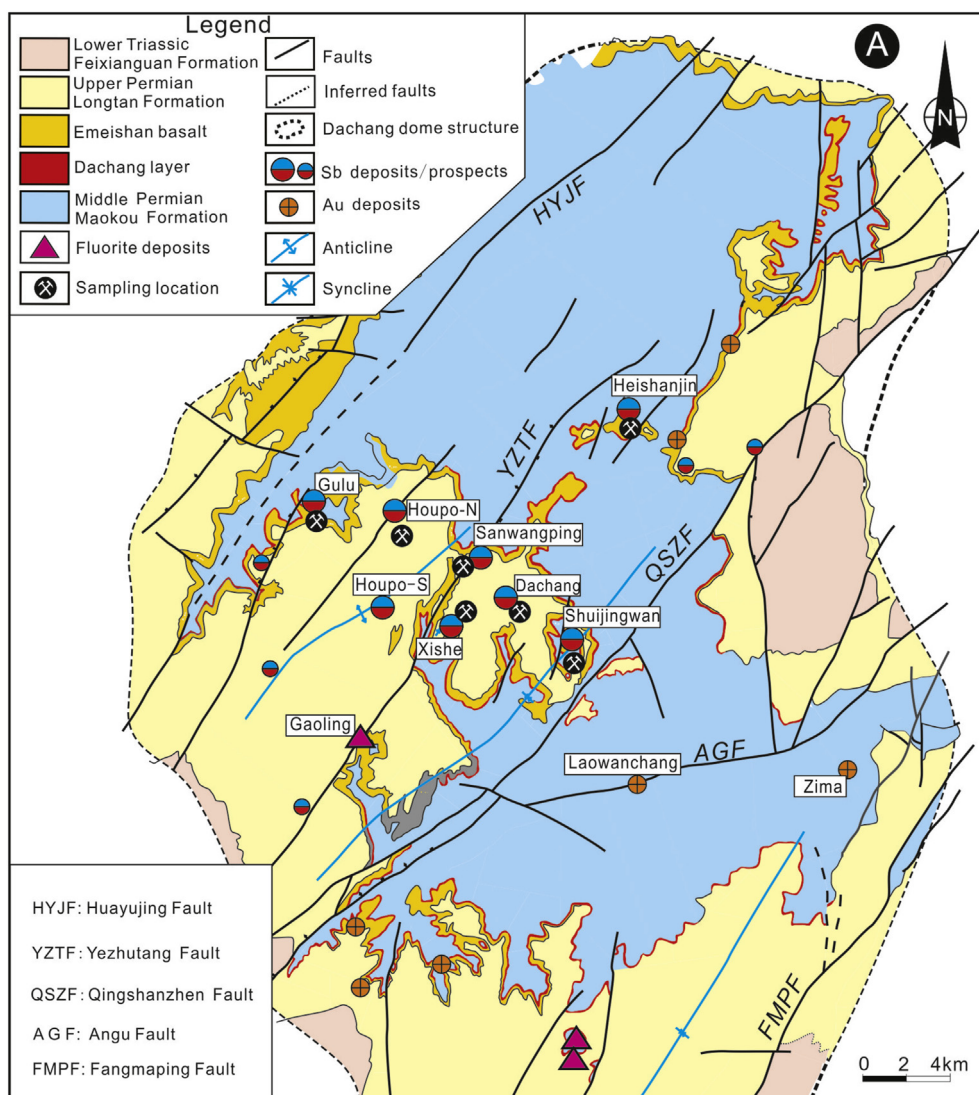
Fig. 3. Geologic map of the Qinglong deposit (modified after Chen et al., 2018).

relatively high porosity, and is the main Sb ore host. The upper unit comprises tuff and carbonaceous mudstone, and contains abundant pyrite. The Emeishan flood basalt contains a complex assemblage of reducing carbonaceous clastic sedimentary rocks deposited in a marginal basin environment in the Late Permian (~260 Ma) (Xu et al., 2004). The Longtan Formation comprises interbedded sandstone and shale. The Lower Triassic Feixianguan Formation is dominated by turbidites including oolitic/muddy limestone and siltstone. The Qinglong deposit, similar to many Au deposits in the NWYB, is structurally located in a dome with complex NE- and E-striking faults (Fig. 3).

At Qinglong, Sb ores contain euhedral-subhedral stibnite, jasperoid quartz, and fluorite (Fig. 5A), and sub-economic Sb–Au mineralization is hosted dominantly by veins of quartz, arsenian pyrite and fine-grained stibnite (Fig. 5B–D). Alteration styles associated with the Sb and Au mineralization include silicic and fluorite (Fig. 5A–D). The lensoidal quartz-stibnite-fluorite-type orebodies are commonly crosscut by quartz-stibnite-pyrite-type veins (Fig. 5E and F), indicating that the Sb ores were formed before the Sb–Au ores. Based on field crosscutting relationships at Qinglong and mineral paragenesis, three alteration/mineralization stages (pre-ore, early-ore and late-ore) are identified (Fig. 6). The pre-ore stage is characterized by framboidal/biological-cluster pyrite and organic matter (Fig. 7A), which were likely formed during the Permian carbonate/clastic ore-host sedimentation and diagenesis (Hou et al., 2016; Zhao et al., 2018). Two types of stibnite are identified: Stibnite 1

(Stb1) is euhedral coarse-grained and coexists with quartz and fluorite at early-ore stage (Figs. 5A and 7B), whereas stibnite 2 (Stb2) is mostly subhedral fine-grained, and coexists with zoned pyrite in late-ore-stage quartz veins (Figs. 5C and 7C).

The Qinglong deposit contains a number of (un)zoned pyrite types, with zoned pyrite being the dominant gold host. The zoned pyrite is subhedral fine-grained (10–40 μm) or coarse-grained (50–300 μm) (Figs. 7D–F), and consists of dark cores and zoned rims (Fig. 7F) in BSE images. It commonly coexists with stibnite 2 (Stb2) and occurs mostly in gold-stibnite ores (Figs. 5C, D and 7C) in the Dachang layer. Three pyrite generations in the zoned pyrite have been recognized based on the grain size, texture, and paragenetic sequence: pyrite 1 (Py1) in the core is overgrown by pyrite 2 (Py2) and pyrite 3 (Py3) on its rim (Fig. 7F). BSE images show that Py2 is present in the inner rim and has a distinct As-rich zone (Fig. 7F), whereas Py3 is mainly present in the outer rim around Py2 (Fig. 7F). Therefore, we conclude that the sulfide paragenetic sequence at Qinglong: Py1 → Stb1 → Py2 → Py3-Stb2.

2.3. Other gold deposits in the NWYB

Ore deposit geology of major Au deposits in the NWYB is summarized below (e.g., Su et al., 2008, 2009a,b, 2012, 2018; Hou et al., 2016; Hu et al., 2018a,b): Shuiyindong is one of the largest (~100 t at 5 g/t Au) stratabound gold deposits in China (Su et al., 2012). Disseminated
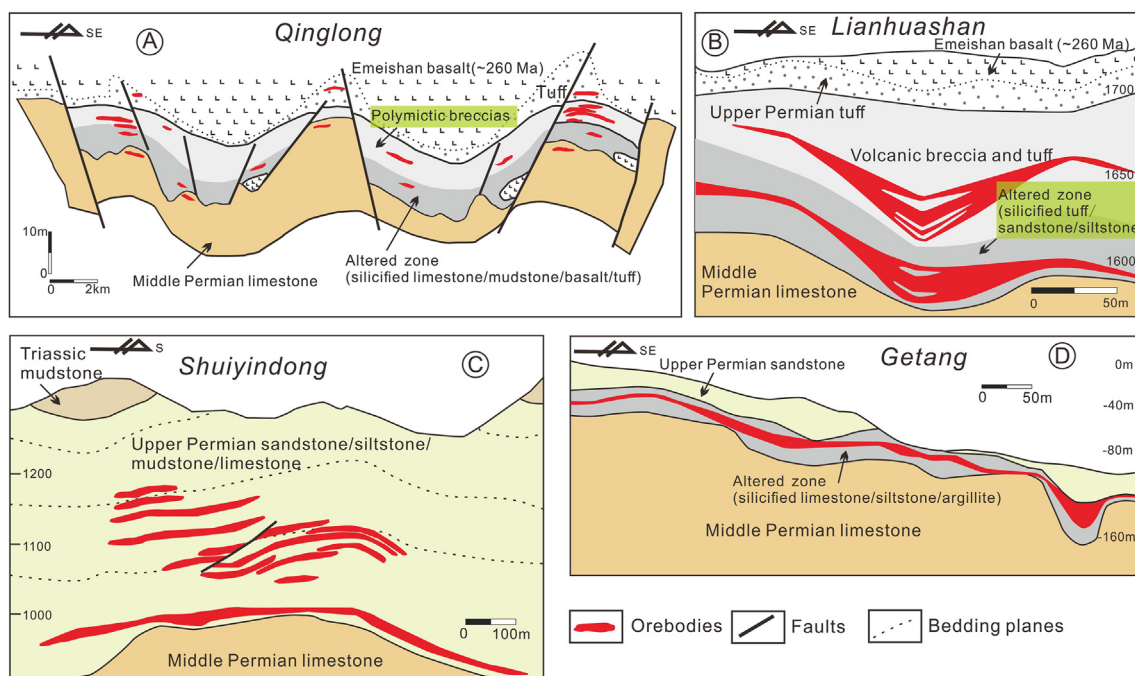
Fig. 4. Geological cross-sections of major gold and antimony deposits in the northwestern margin of the Youjiang basin, showing that these deposits are mainly hosted by the Upper Permian limestone and sandstone. (A) Qinglong Sb(Au) deposit, modified after Chen et al. (2018); (B) Lianhuashan Au deposit, modified after Hu et al. (2018b); (C) Shuiyindong Au deposit, modified after Hou et al. (2016); (D) Getang Au deposit, modified after Hu et al. (2018a).

(arseno)pyrite mineralization is hosted in the Upper Permian Longtan Fm. bioclastic limestone (Fig. 4C), near the axis of the Huijiabao anticline (a narrow corridor <20 km long and 5 km wide; Hou et al., 2016). The Taipingdong and Nayang deposits are also located in the Huijiabao anticline, in which the major Au orebodies occur in the Longtan Fm. decarbonatized carbonates and silicified siltstone (Hou et al., 2016). The Getang gold deposit (resource: ~30 t at 5.1 g/t Au) has its Au mineralization primarily confined to the interlayer fracture zones at the base of the Longtan Formation, and is hosted in the silicified, brecciated limestone and argillite (Figs. 3D and 4D; Zhang et al., 2003; Hu et al., 2018a). For these above-mentioned gold deposits, the gold is invisible and resides in zoned arsenian pyrite and arsenopyrite (Su et al., 2009a, 2018). In addition, a number of gold deposits (e.g., Lianhuashan) have been discovered in the Emeishan basalt in the NWYB (Fig. 4B; Hu et al., 2018b). Arsenian pyrite is also the main ore mineral in the Lianhuashan deposit.

As mentioned above, Sb mineralization in the NWYB likely occurred in similar age and tectonic setting to the regional Au mineralization. Furthermore, these Au and Sb deposits have similar ore-related alterations (decarbonate, silicic and argillic), ore mineral assemblage (pyrite + arsenopyrite + stibnite), and ore host (Upper Permian-Middle Triassic sequence) (Peters et al., 2007; Cline et al., 2013; Hou et al., 2016; Chen et al., 2018; Su et al., 2018).

3. Samples and analytical methods

3.1. Samples

Ore samples were collected from field outcrops and underground tunnels of the Qinglong deposit (Dachang, Shuijingwan, Sanwangping, Houpo-North, Heishanjin and Gulu ore blocks) (Fig. 3). Mineral contents and textures of the ore-related pyrite and stibnite were studied on 26 hand specimens and 18 thick sections. Eight representative polished thick sections were analyzed using scanning electron microscopy (SEM) for the pyrite and stibnite mineral assemblages. After that, fragments (2–5 mm diameter) of the thick sections (with multiple pyrite and stibnite types) were cut out with a micro-drill and mounted onto 25-mm

diameter epoxy discs for NanoSIMS sulfur isotope and LA-ICP-MS trace-element analyses (Fig. 7A). EPMA was then conducted on the NanoSIMS analysis spots to measure the sulfide major/minor elemental compositions.

3.2. Analytical methods

Secondary electron and BSE images were collected using a JSM-7800F SEM to identify minerals and provide semi-quantitative geochemical measurements. EPMA was conducted with a JXA8530F-plus electron microprobe under the operation conditions of 15 kV, 10 nA, 1 μm-diameter beam size, and measurement time of 10 s (sample) and 5 s (background). The following synthetic standards were used: pyrite (FeS_2) for Fe and S, arsenopyrite (FeAsS) for As, skutterudite ([(Co, Ni, Fe)As_{3-x}]) for Co, pentlandite ((Fe,Ni)$_9S_8$) for Ni, gold (Au^0) for Au, stibnite (Sb_2S_3) for Sb, (silver) Ag^0 for Ag, cuprite (Cu_2O) for Cu, bismuth selenide (Bi_2Se_3) for Se, rutile (TiO_2) for Ti, and sphalerite (ZnS) for Zn. Detection limits are 112 ppm for Fe, 141 ppm for Zn, 113 ppm for Ni, 83 ppm for Co, 129 ppm for Cu, 89 ppm for Ti, 371 ppm for As, 167 ppm for Se, 69 ppm for S, 328 ppm for Au, 124 ppm for Ag and 147 ppm for Sb. The analytical errors are <1% for Fe and S, and <10% for As, Ni, Au, Co, Ag, Cu, Sb, Se, Ti and Zn. The SEM and EPMA analyses were performed at the State Key Laboratory of Ore Deposit Geochemistry, Institute of Geochemistry (IG), Chinese Academy of Sciences (CAS).

LA-ICP-MS pyrite trace element analysis was conducted at the Tuoyan Testing Technology Co. Ltd. (Guangzhou, China). Laser sampling was performed using a GeolasPro laser ablation system with a COMPexPro 102 ArF excimer laser (wavelength of 193 nm and maximum energy of 200 mJ) and a MicroLas optical system. An ICAP RQ ICP-MS instrument was used to acquire ion signal intensities. Helium was used as the carrier gas. Argon was used as the make-up gas and mixed with the carrier gas via a T-connector before entering the ICP. The spot size and frequency of the laser were set to 24 μm and 5 Hz, respectively. The data were calibrated against the MASS-1 synthetic pyrite and NIST 610 standards, and ^{57}Fe was used as the internal standard. Data processing, including offline selection and integration of background/analyzed signals, time-drift correction and calibration for trace element analysis, was performed
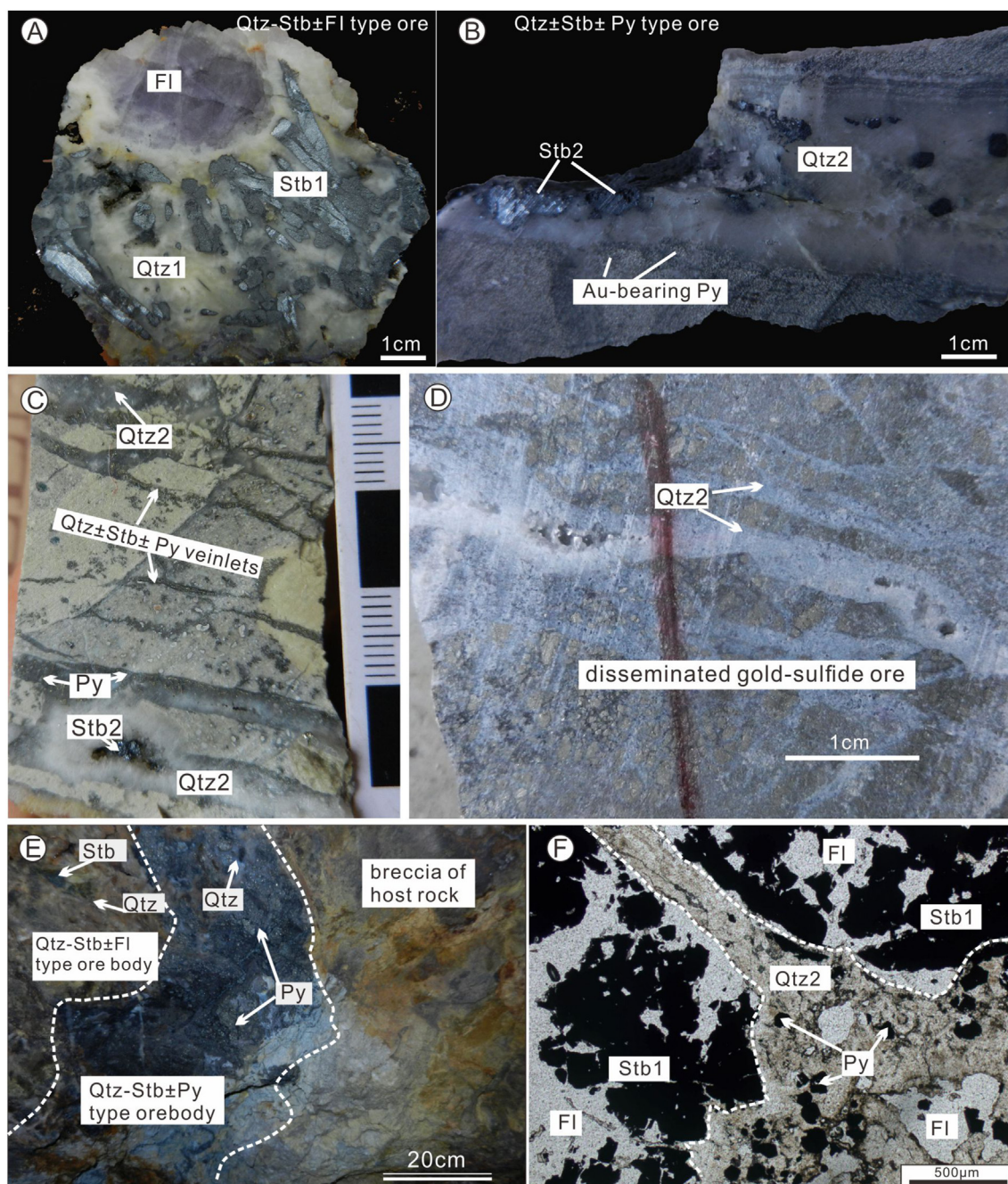
Fig. 5. Representative photographs showing two main types of Sb–Au ores at Qinglong. (A) Hand-specimen of stibnite-quartz-fluorite ores, showing euhedral coarse-grained stibnite that coexists with white quartz and purple fluorite. (B and C) Hand-specimen of pyrite-stibnite-quartz vein filled in pyritized tuff and argillic-altered basalt. (D) Disseminated gold-sulfide ore cut by quartz veinlets. (E and F) Vein-type Qtz-Stb ± Py ores crosscut Qtz-Stb ± Fl ores. Abbreviations: Py – pyrite; Qtz – quartz; Stb – stibnite; Fl – fluorite. A and B from Chen et al. (2018).

with the Excel-based software ICPMSDataCal (Liu et al., 2008).

In-situ trace element mapping and pyrite S-isotope analysis were conducted with a CAMECA NanoSIMS 50L instrument at the Institute of Geology and Geophysics, CAS (Beijing). The FC-EM-EM model was used to meet the spatial resolution requirements (Yang et al., 2015). ^{32}S was counted with a Faraday Cup (FC), and ^{34}S and other elements were counted with electronic multipliers (EMs) (Zhang et al., 2014). The Sonora pyrite was used as a running standard for sulfur isotopes ($\delta^{34}S_{V\text{-CDT}}$: +1.61‰; and $\delta^{33}S_{V\text{-CDT}}$: +0.83‰; Farquhar et al., 2013), and were analyzed twice to thrice for every six to eight Qinglong pyrite analyses. High-spatial-resolution images of six elements or isotopes (^{75}As, ^{34}S, $^{63}Cu^{32}S$, ^{80}Se ^{197}Au, and $^{208}Pb^{32}S$) were simultaneously obtained.

The peaks were calibrated with working references of chalcopyrite ($^{63}Cu^{32}S$), arsenopyrite (^{75}As), $FeSe_2$ (^{80}Se), Au foil (^{197}Au), and galena ($^{208}Pb^{32}S$). The measurement processes are as follows: (1) thin sections were carbon-coated and placed in the sample compartment; (2) a 0.3 μm and 7 pA Cs^+ primary ion beam rastered across the sample surface, sputtering out positive and negative secondary ions, which were separated in the magnetic field based on their mass-to-charge ratios; (3) the signals (6 elements/isotopes) were detected by six FC or EMs; and (4) a 20 μm × 20 μm analysis area was ablated. Detailed analytical procedures were the same as those outlined in Zhang et al. (2014) and Yang et al. (2015). In-situ stibnite S-isotope analyses were performed using femtosecond laser ablation MC-ICP-MS at the State Key Laboratory of
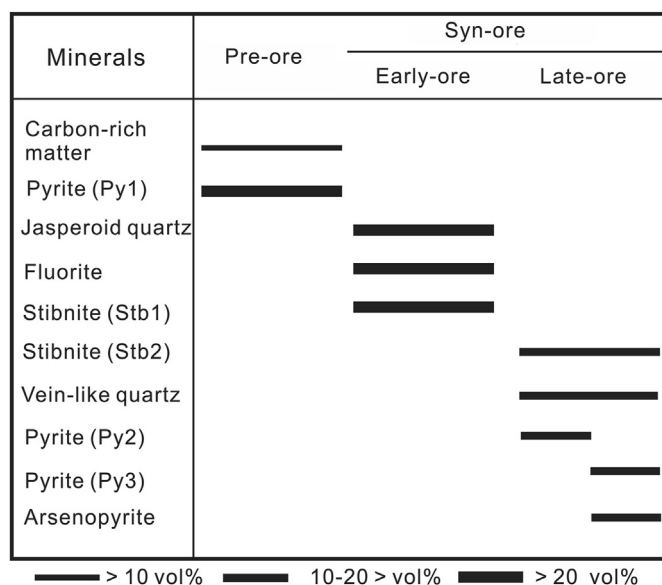
Fig. 6. Mineral paragenesis of the Qinglong Sb(Au) deposit.

Continental Dynamics, Department of Geology, Northwest University (Xi'an, China). A RESOlution M − 50 laser ablation system (ASI, Australia), equipped with a 193 nm ArF CompexPro102 excimer laser (Coherent, USA), a large double-cell sample chamber, and a computer-controlled, high precision X–Y sample positioning stage was employed. The NBS123 ($\delta^{34}S_{V-CDT}$ = +17.8‰ ± 0.2‰, 2SD), Py-4 ($\delta^{34}S_{V-CDT}$ = +1.7‰ ± 0.3‰, 2SD), Cpy-1 ($\delta^{34}S_{V-CDT}$ = +4.2‰ ± 0.3‰, 2SD) and CBI-3 ($\delta^{34}S_{V-CDT}$ = +28.5‰ ± 0.4‰, 2SD) standards were used in the analysis. The spot size used in this study was 30 μm. Detailed analytical procedures were as described by Yuan et al. (2018).

4. Results

4.1. Chemical compositions of pyrite and stibnite

LA-ICP-MS trace element concentrations of Py1 (16 spots), Py2 (12 spots) and Py3 (18 spots) are listed in Table 1 and illustrated in Figs. 8 and 9, and EPMA major/minor element data for Stb1 and Stb2 are listed in Table 2. Arsenic is the most abundant minor element in pyrite: Py1 (4.2–920 ppm, mean 116 ppm), Py2 (21,800–51,300 ppm, mean 41,033 ppm) and Py3 (544–65,000 ppm, mean 12,674 ppm). Gold contents are mostly below the LA-ICP-MS detection limit (bdl: ~2 ppm) for Py1, but Py2 (9.1–20.6 ppm, mean 15.7 ppm) and Py3 (bdl to 21.7 ppm, mean 4.4 ppm) have elevated Au contents. Antimony contents have a wide range, i.e., bdl to 22.6 ppm for Py1, 1690–5230 ppm (mean 3292 ppm) for Py2, and 51–6400 ppm (mean 1809 ppm) for Py3. Copper contents are of 1.2–32.4 ppm (mean 11.8 ppm) for Py1, 430.0–951.0 ppm (mean 641.0 ppm) for Py2, and 15.5–830.0 ppm (mean 220.0 ppm) for Py3. Meanwhile, the Ag contents are bdl for Py1, 35.6–77.0 ppm (mean 48.0 ppm) for Py2, and 1.4–88.0 ppm (mean 15.6 ppm) for Py3. EPMA indicates that Stb1 has lower As (0.12–0.30 wt.%, mean 0.20 wt.%, n = 29) than Stb2 (0.91–1.20 wt.%, mean 1.05 wt.%, n = 10). In summary, the pre-ore Py1 is featured by having the lowest Au, As, Sb, Cu and Ag contents (commonly bdl), compared to the syn-ore Py2 and Py3. Early-ore Py2 is richer in these elements than late-ore Py3. In addition, the average Co/Ni values increase from 0.31 in Py1, through 1.75 in Py3, to 1.97 in Py2.

4.2. Nano-scale elemental and sulfur isotope distribution in sulfides

Calculated $\delta^{34}S$ values of 70 spots on six auriferous pyrite samples from Qinglong are listed in Table 3. Submicron-resolution NanoSIMS images of S-isotopes and trace elements (^{75}As, ^{34}S, $^{63}Cu^{32}S$, ^{80}Se, ^{197}Au

and $^{208}Pb^{32}S$) for Py1, Py2 and Py3 are shown in Figs. 10 and 11. The results reveal that the pyrites have systematic zoning of Au, As, Cu and S (Fig. 10), similar to those reported in the Turquoise Ridge Carlin-type Au deposit in Nevada (Barker et al., 2009) and the Nannigou Au deposit in the Youjiang basin (Yan et al., 2018). Arsenic and gold are closely related in many gold deposits, including Carlin-type (Cline, 2001; Reich et al., 2005; Xing et al., 2019), orogenic (Large et al., 2009), and epithermal deposits (Deditius et al., 2014), and are both hosted in Fe-sulfides (pyrite, marcasite, and arsenopyrite). This is partly because As contents control Au accumulation (Fleet and Mumin, 1997; Deditius et al., 2014; Xing et al., 2019, and reference therein). The higher the local arsenic content, the greater the defect density around the arsenic occurrence, and hence more gold can be accommodated within these As-rich areas and dispersed across the arsenian pyrite grain (Gopon et al., 2019). In the NanoSIMS Au–As distribution maps (Fig. 11), zoning in the Au-bearing pyrite is clearly visible as broad alternating bands of As-rich, As-poor and As-free zones (Table 3). Arsenic-rich zones are common in Py2 and Py3, and have elevated Au, Cu and Se concentrations (Fig. 10). Arsenic-poor zones are most common in Py1 and Py2, with low Au and Cu concentrations. Arsenic-free zones occur only in Py1 and have very low trace element contents.

At Qinglong, sulfur isotope compositions of Au-bearing pyrites range from −18.9‰ to +18.1‰ (Fig. 12). Each pyrite zone has a distinct $\delta^{34}S$ range (Fig. 12): As-rich zone: 6.9‰ to +6.1‰ (mostly −4.2‰ to +1.6‰, mean + 1.1‰ ± 3.5‰, n = 33); As-poor zone: 9.2‰ to +15.3‰ (mostly 4.4‰–11.8‰, mean + 7.8‰ ± 6.0‰, n = 20); As-free zone: 18.9‰ to +18.1‰ (mostly 2.7‰–7.5‰, mean + 3.3‰ ± 9.0‰, n = 20). The sulfur isotope data of 23 stibnite samples and 11 spots of fs-LA-MC-ICP-MS are listed in Table 4. The $\delta^{34}S$ values of Stb 1 (−4.7‰ to +0.3‰, mean −2.3‰ ± 1.5‰, n = 17) and Stb 2 (−6.6‰ to +3.2‰, mean −2.0‰ ± 2.8‰, n = 17) have an almost identical range (Fig. 13A), indicating that the sulfur of the two ore-stages was probably derived from the same source.

4.3. Other Carlin-like Au deposits in the NWYB

In this paper, we compiled in-situ sulfur isotope data of the Au-bearing pyrites from the Shuiyindong (Tan et al., 2015; Hou et al., 2016; Xie et al., 2018b), Taipingdong, Nayang (Hou et al., 2016), Getang (Hu et al., 2018a) and Lianhuashan (Hu et al., 2018b) Carlin-like gold deposits in the NWYB. To better characterize the ore-fluid sources and compare with those of Qinglong, we select only the $\delta^{34}S$ values of hydrothermal As–Au-rich zones of the Au-bearing pyrite. Common textures and ore-related elemental contents (e.g., Au, As, Cu and Sb) of the Au-bearing pyrite form these deposits are summarized in Appendix I.

In the NWYB, $\delta^{34}S$ values of the As–Au-rich zones of the early-ore Au-bearing pyrite (−2.8‰ to +8.4‰, mean + 1.1‰ ± 2.4‰, n = 87) and arsenopyrite (−0.9‰ to +2.1‰, mean + 0.2‰ ± 0.8‰, n = 13) from the Carlin-like deposits have relatively narrow ranges (Fig. 13B). Previous studies on the Carlin-like gold deposits in the Youjiang basin showed that the realgar, orpiment and stibnite were formed in the late-ore stage with relatively narrow $\delta^{34}S$ ranges: stibnite: 4.9‰ to +1.8‰ (mean −1.5‰ ± 2.6‰, n = 7); realgar: +1.8‰ to +5.3‰ (mean + 3.5‰ ± 1.1‰, n = 15); orpiment: +2.5‰ to +3.0‰ (mean + 2.7‰ ± 0.2‰, n = 4) (Fig. 13B; Su et al., 2008, 2012, 2018; Xie et al., 2018b).

5. Discussion

5.1. Relationship between gold and antimony mineralization

At Qinglong, As contents range widely (from bdl to 6.5 wt.%) in Au-bearing pyrites, and are significantly higher in the syn-ore Py2 and Py3 than the pre-ore Py1. In the As vs. Au–Cu–Sb–Ag diagrams (Figs. 8B–E), positive correlations are present in Py2 and Py3 but absent in Py1. The LA-ICP-MS mapping also indicates high Au, Cu, Sb and Ag contents in the As-rich band (Py2) of the zoned pyrites (Fig. 9). In addition, early-ore
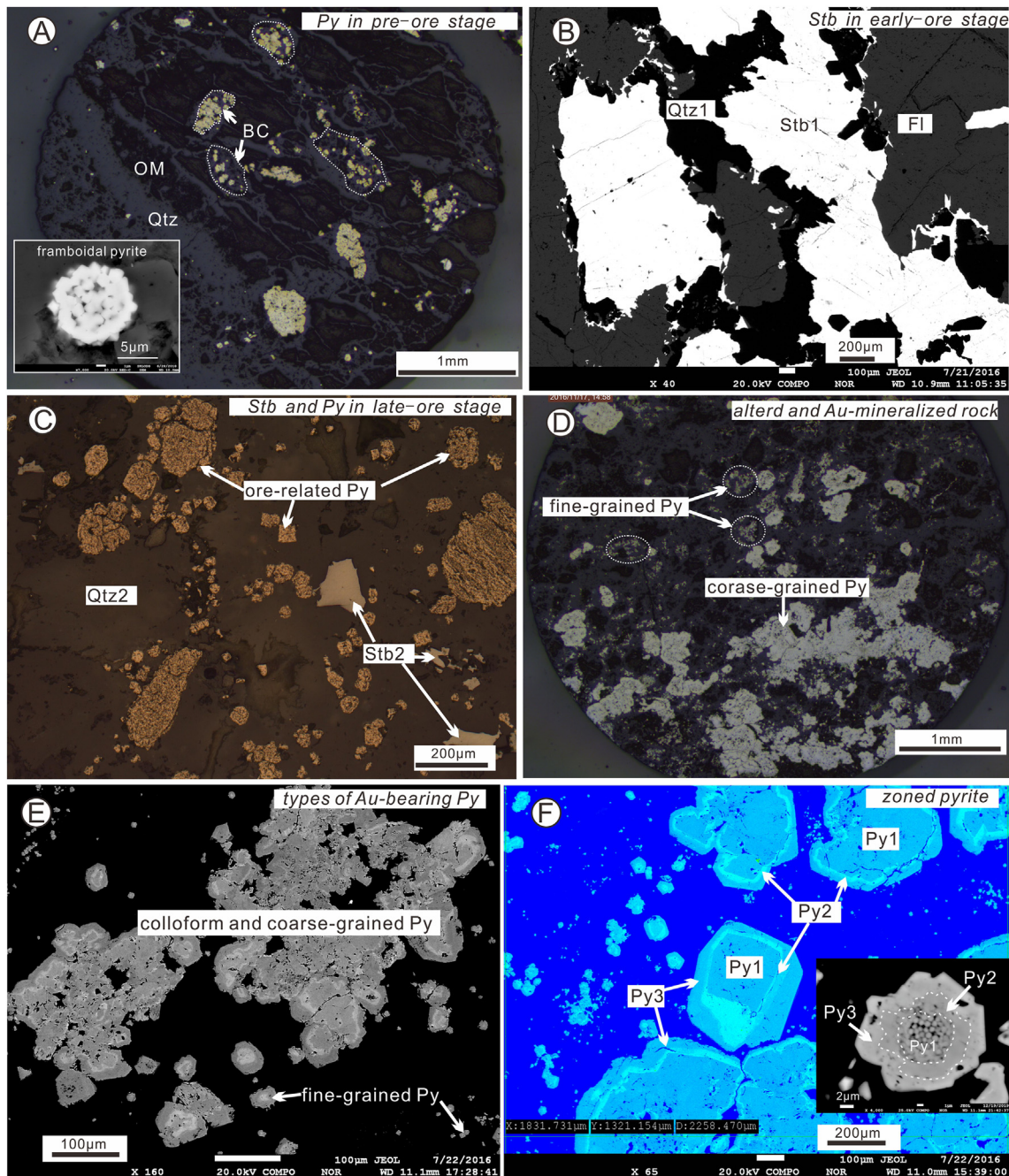
Fig. 7. Photomicrographs of major ore-related minerals and their relationships in the Qinglong deposit. (A) Reflected-light image of framboidal pyrite occur as biological cluster (BC) and intergrown with organic matter (OM). (B) Backscattered electron (BSE) image of euhedral-subhedral stibnite, fluorite and quartz in Sb-rich ores. (C) Reflected-light image of stibnite and pyrite in quartz veins. (D) Reflected-light image of coarse-grained pyrite and fine-grained pyrite in Au ores. (E) BSE image of colloform and coarse-grained pyrite. (F) Colorized BSE image of zoned pyrite with Py1 core, As-rich Py2 inner rim and Py3 outer rim. Minor pre-existing framboidal pyrite was altered by ore-stage hydrothermal fluids (bottom right). Abbreviations given in Fig. 5.

Stb1 has lower As than late-ore Stb2 at Qinglong (Fig. 8F), which indicates that the As contents increase gradually from the early-ore to late-ore stage. All LA-ICP-MS spots in Py2 and Py3 have similar As/Au (1:100 to 1:1000), As/Sb (1:10 to 1:100), As/Cu (1:10 to 1:100) and As/Ag ratios (1:100 to 1:1000) (Figs. 8B–E), suggesting that the As–Au–Sb–Cu–Ag may have been leached and transported together from the same metamorphic/sedimentary source. Consequently, we infer that the ore-forming fluids are distinctly enriched in As–Au–Sb–Cu–Ag, and the progressive As increase in pyrite has probably caused the increase of other ore elements.

Pyrite Co/Ni ratio is sensitive to hydrothermal environmental change,

and can be used as a metallogenic indicator for some hydrothermal ore deposits (Bralia et al., 1979; Cook et al., 2009). At Qinglong, the Co/Ni ratios of pre-ore Py1 (mean 0.31) and syn-ore Py2 and Py3 (mean 1.97 and 1.75, respectively) are markedly different (Fig. 8A). Low Co/Ni ratios (<1) are commonly attributed to a sedimentary/diagenetic origin (Bralia et al., 1979), whereas high Co/Ni ratios (>1) are commonly attributed to an epithermal hydrothermal origin (Chen et al., 2009).

For the Carlin-like gold deposits in the NWYB, arsenian pyrite is also a major host for gold. Many studies have shown that arsenian pyrites are commonly zoned and have multiphase overgrowth (e.g., Peters et al., 2007; Su et al., 2008, 2009a,b, 2012, 2018; Chen et al., 2015; Tan et al.,

Table 1
Trace elements concentrations of Au-bearing pyrites by LA-ICP-MS analysis from the Qinglong Sb(Au) deposit (in ppm).

Type	Sopts	Co	Ni	Cu	Zn	As	Se	Ag	Sb	Ba	W	Au
Py1	PY-DC4-1	4.04	39.1	2.59	0.75	16	bdl	bdl	bdl	0.015	bdl	bdl
Py1	PY-DC4-2	4.25	40.6	1.21	1.08	4.92	bdl	bdl	bdl	bdl	bdl	bdl
Py1	PY-DC4-3	9.37	85.7	3.8	0.78	34.1	bdl	0.026	bdl	0.86	bdl	bdl
Py1	PY-DC4-4	6.01	48.8	3.26	0.7	0.59	bdl	bdl	bdl	0.23	bdl	bdl
Py1	PY-DC4-5	2.79	26	2.78	1.53	26	bdl	bdl	bdl	0.046	bdl	bdl
Py1	PY-DC4-6	11.5	109.8	3.26	1.16	40.8	1	bdl	bdl	bdl	bdl	bdl
Py1	PY-DC4-7	59.6	539	32.4	2.43	378	bdl	0.078	11.9	1.43	0.056	bdl
Py1	PY-DC4-8	8.5	63.9	3.43	1.31	4.2	bdl	0.036	0.45	1.09	bdl	bdl
Py1	PY-DC4-9	8.7	3.3	26.2	1.92	186	bdl	0.76	22.6	0.47	0.1	0.032
Py1	PY-DC4-10	4.41	37	3.51	1	14.5	bdl	0.19	0.65	0.01	bdl	bdl
Py1	PY-DC4-11	30.6	157	11.4	1.55	108	bdl	bdl	4.3	1.7	bdl	0.01
Py1	PY-DC4-12	4.02	31.5	11.8	1.97	10.7	0.5	0.13	0.28	0.5	bdl	bdl
Py1	PY-DC4-13	8.13	62.2	12.4	3.8	19.1	bdl	0.37	bdl	0.96	bdl	bdl
Py1	PY-DC4-14	11.8	109	19.7	2.8	81	0.1	0.34	bdl	2.18	0.49	bdl
Py1	PY-DC4-15	5.91	55.5	19.2	5.2	21.7	bdl	0.55	bdl	3.38	0.12	bdl
Py1	PY-DC4-16	13.3	21	32	3.2	920	2.9	0.08	60	4.1	4.9	0.53
Py2	PY-LS-5	214	108	658	4.39	30400	70.1	35.6	2020	8.9	4.55	10.1
Py2	PY-LS-1	50.5	31.4	951	1.94	40200	27	47.3	1690	320	2.1	13.8
Py2	PY-LS-6	181	78	570	2.51	21800	37.9	37.8	1690	6.2	7.9	9.1
Py2	PY-LS-9	81	43.6	512	3.5	40500	16	54.9	4410	29.4	6.55	14.9
Py2	PY-LS-16	116	36.7	650	3.22	40800	25.4	77	4650	104	1.92	17.3
Py2	PY-LS-18	106	53	660	2.57	47500	39.3	51.3	2740	147	6.7	16
Py2	PY-LS-19	81	39.2	430	2.88	37000	75.5	39.8	2780	1190	5.01	14.7
Py2	PY-LS-20	63	38.1	558	2.9	44300	30.1	49	2760	89	3.9	19
Py2	PY-LS-21	71.2	35	614	3.35	51300	78	50	2320	117	2.3	20.4
Py2	PY-LS-23	64	55.2	787	4.8	41200	59	42.5	4080	10.3	5	18.6
Py2	PY-LS-24	96	61.4	847	4.33	50600	70	43.6	5130	24	1.22	20.6
Py2	PY-LS-27	235	107	454	6.37	46800	73.6	53.1	5230	26.2	12.04	13.9
Py3	PY-LS-13	609	316	57	6.11	1163	118.3	3.51	2940	16.6	19.8	0.043
Py3	PY-LS-12	69.1	35.3	36.5	2.78	544	63.5	1.37	1230	11.8	9.3	bdl
Py3	PY-LS-26	556	225	76	3.5	2730	85.6	9.5	1370	2.3	1.95	0.43
Py3	PY-LS-25	148	91	33.8	1.7	2110	76.4	3.4	123	5.3	0.91	0.28
Py3	PY-LS-29	105	103	54	1.26	959	47	2.57	51	4	0.258	0.049
Py3	PY-LS-14	64.4	31.7	15.5	5.4	509	30	0.38	145	6.4	1.33	bdl
Py3	PY-LS-7	76.9	49.4	20.5	7.1	789	69.3	0.88	56.4	2.2	0.64	0.175
Py3	PY-LS-3	469	247	25	8.9	791	112	0.34	10.8	2.07	0.35	0.017
Py3	PY-LS-2	402	201	27	2.41	3700	125.7	3.4	108	3.5	1.02	0.173
Py3	PY-LS-4	512	240	204	3.92	13800	93.3	14.5	1780	10.4	3.26	4.65
Py3	PY-LS-10	229	124.5	69.7	4.74	6650	63	13.1	3560	4.28	4.62	1.56
Py3	PY-LS-11	263	145	42.9	6.4	2240	59.9	3.13	61	2.02	1.63	0.067
Py3	PY-LS-15	120	57.6	590	5.5	65000	48.9	88	6300	26	1.19	21.7
Py3	PY-LS-22	221	113	51	9	1430	86.7	3.26	6400	19.5	24	0.021
Py3	PY-LS-17	2.96	5.2	403	1.27	18910	26.3	10.2	1040	4	11.1	2.17
Py3	PY-LS-28	132	74.6	830	5.4	36700	60.5	35.1	4800	1560	1.01	14.8
Py3	PY-LS-8	20.6	37.4	653	1.75	28800	7.6	57.9	825	0.8	1.61	11.4
Py3	PY-LS-30	78	34.2	766	2.07	41300	40.9	29.6	1770	85	6	13

Note: bdl = below the detection limit.

2015; Hou et al., 2016; Yan et al., 2018; Li et al., 2020b). These zoned arsenian pyrites consist of an As-rich rim on an As-poor core. The As-rich (2–11 wt.%) rim is hydrothermal and Au-rich (<4000 ppm at Shuiyindong; Su et al., 2018). In contrast, the As-poor (<1 wt.%) core is diagenetic and Au-poor (<10 ppm) (Appendix I). In addition, the fluid inclusions from the early-ore hydrothermal quartz that paragenetically related to these pyrite rims contain As (~200 ppm) and Sb (~200 ppm), and up to 6 ppm Au (Su et al., 2009a). During the hydrothermal alteration, the late Au-rich pyrite precipitation was followed by the precipitation of Sb–As-rich minerals (e.g., realgar, orpiment and stibnite) (Su et al., 2018). Fluid inclusions in the stibnite-realgar-quartz veins of the Yata gold deposit (in Youjiang basin) also contain up to 90 ppm Sb and 250 ppm As (Su et al., 2009a). These characteristics lead to the conclusion that the Au, Sb and As were most likely transported together in the same fluid.

5.2. Sulfur sources

NanoSIMS mapping and LA-ICP-MS analysis reveal that most Py2 and Py3 grains have elevated Au and As contents, and Py2 has the highest As–Au–Sb–Cu–Ag contents (Fig. 9). Hence, $\delta^{34}S$ values of the Py2/Py3 As-rich zones can best represent those of the ore-forming fluids. The $\delta^{34}S$ values of the Py2/Py3 As-rich zones are relatively low and cluster around 0‰ (−6.9‰ to +6.1‰, mostly −4.2‰ to +1.6‰; Figs. 12 and 13A). In contrast, Py1/Py2 As-poor/-free zones have a much wider $\delta^{34}S$ range (−18.9‰ to +18.1‰, mostly +3‰ to +12‰; Fig. 12). The EPMA major/minor elemental data (collected on the same spots as the NanoSIMS S-isotope analyses) reveal that decreasing pyrite $\delta^{34}S$ values is accompanied by increasing As contents, and the $\delta^{34}S$ range becomes much narrower (−5‰ to +5‰) in high As contents (Fig. 14; Appendix II). It is well known that Au has a close correlation with As in Carlin-type/like gold deposits (Reich et al., 2005; Xing et al., 2019), which is consistent with increased local arsenic concentrations that enhanced the ability of arsenian pyrite to host dispersed gold (Kusebauch et al., 2019). Xing et al. (2019) proposed that As-poor fluids are also able to form high-As pyrite through extensive alteration. Therefore, the pyrite As-rich zones were likely formed by extensive hydrothermal alteration with the fluid evolution (Large et al., 2009; Xing et al., 2019).

In low-temperature Sb–Au ore fluids, Au is principally transported as Au-HS complexes (Cline et al., 2005; William-Jones et al., 2009; Su et al., 2018), whilst Sb is mainly transported as bisulfide (Sb$_2$S$_2$(OH)$_0$) complexes (Krupp, 1988; Spycher and Reed, 1989) and/or hydroxybisulfide (HSb$_2$S- 4) complexes (Krupp, 1988; Williams-Jones and Norman, 1997). Hence, S-isotope ratios can shed light on Au–Sb ore fluid sources. The
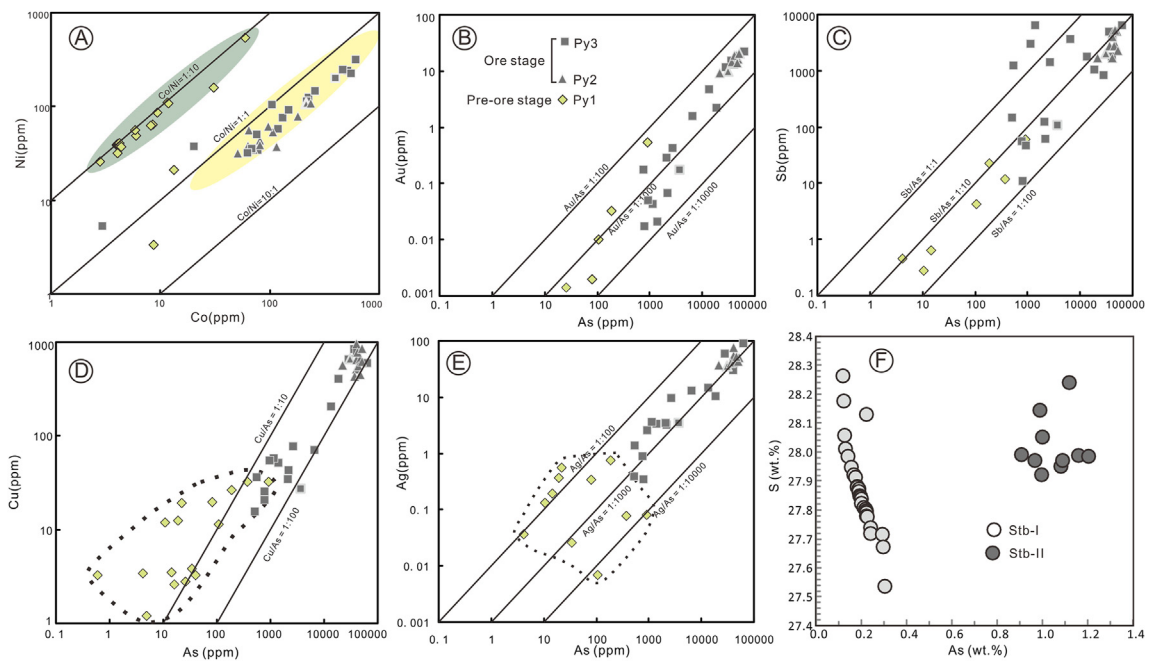
Fig. 8. Binary plots showing selected trace-element contents and ratios of the different types of pyrites and stibnite. (A) Co vs. Ni; (B) As vs. Au; (C) As vs. Sb; (D) As vs. Cu; (E) As vs. Ag (LA-ICP-MS Au-bearing pyrite data); (F) As vs. S (EPMA stibnite data).
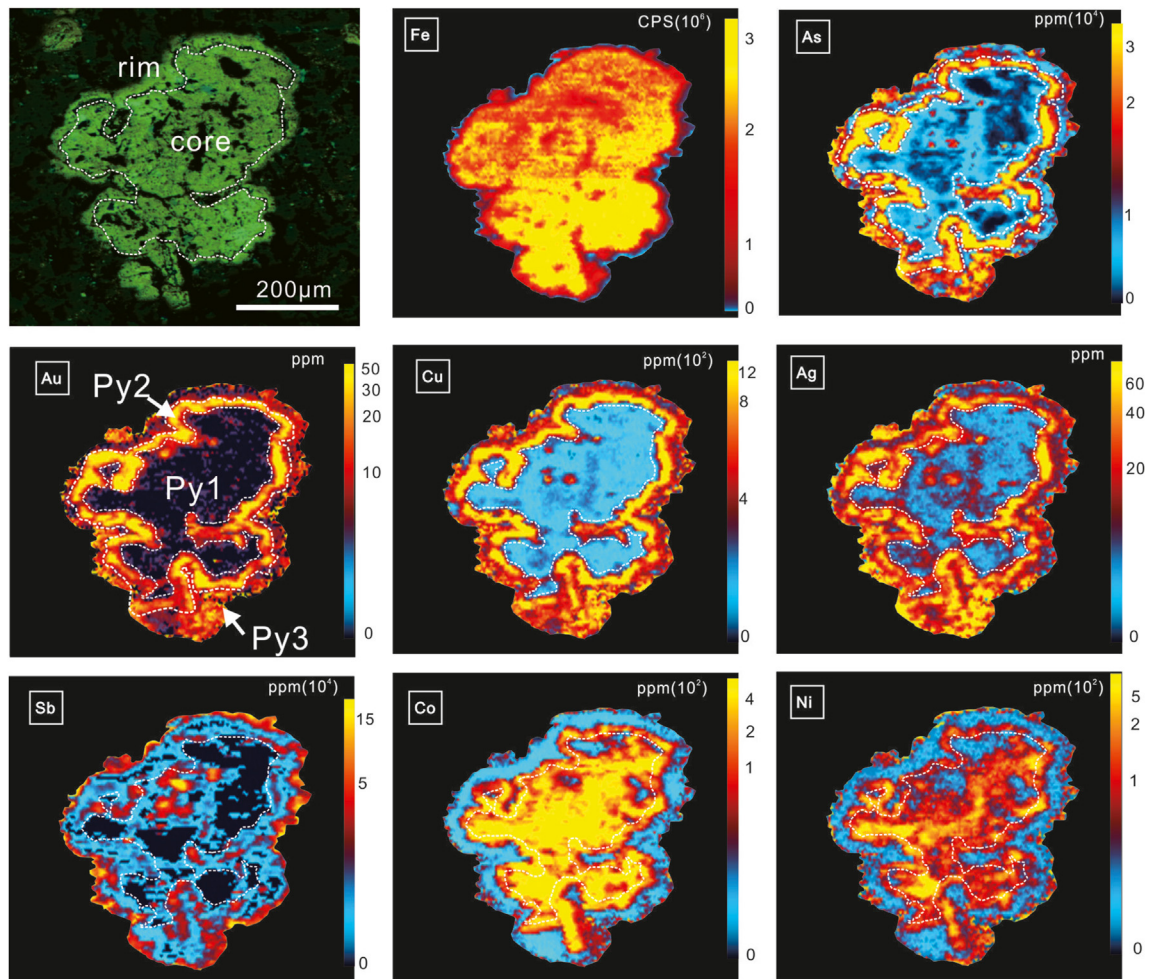

Fig. 9. LA–ICP–MS elemental maps of representative pyrite grains from Qinglong. Scale in counts-per-second (cps).

Table 2
Representative EPMA data of the stibnite from the Qinglong Sb(Au) deposit (in wt.%).

Texture	Sample No.	Grain type	As	Fe	Cu	Zn	S	Au	Pb	Ag	Sb	Total
Corase-grained stibnite in jasperoid Qtz	DSY7-1	Stb1	0.22	0.04	bdl	0.03	28.13	bdl	bdl	bdl	72.12	100.56
	DSY7-1	Stb1	0.12	bdl	bdl	bdl	28.26	bdl	0.08	0.06	72.38	100.91
	DSY7-1	Stb1	0.12	bdl	0.02	bdl	28.18	bdl	bdl	0.03	72.37	100.74
	DSY7-1	Stb1	0.13	bdl	bdl	0.04	28.06	bdl	0.05	bdl	72.15	100.43
	DSY7-1	Stb1	0.13	bdl	bdl	bdl	28.01	bdl	bdl	0.02	72.11	100.27
	DSY7-1	Stb1	0.14	bdl	bdl	bdl	27.98	bdl	0.05	bdl	72.06	100.24
	DSY7-1	Stb1	0.16	bdl	0.07	bdl	27.95	bdl	bdl	bdl	71.98	100.15
Corase-grained stibnite in jasperoid Qtz	DSY7-2	Stb1	0.17	bdl	0.03	0.02	27.92	bdl	bdl	bdl	71.89	100.02
	DSY7-2	Stb1	0.17	bdl	bdl	0.08	27.91	bdl	0.02	bdl	71.89	100.07
	DSY7-2	Stb1	0.18	0.02	bdl	bdl	27.88	bdl	0.02	bdl	71.87	99.97
	DSY7-2	Stb1	0.18	0.02	bdl	0.02	27.88	bdl	bdl	bdl	71.86	99.96
	DSY7-2	Stb1	0.19	bdl	0.02	bdl	27.87	bdl	bdl	bdl	71.86	99.94
	DSY7-2	Stb1	0.19	0.02	bdl	bdl	27.86	bdl	bdl	bdl	71.85	99.93
Disseminated stibnite in jasperoid Qtz	GL-12	Stb1	0.19	0.02	bdl	bdl	27.85	bdl	bdl	0.02	71.80	99.89
	GL-12	Stb1	0.20	bdl	0.08	bdl	27.84	bdl	bdl	bdl	71.80	99.93
	GL-12	Stb1	0.20	bdl	0.03	bdl	27.84	bdl	bdl	bdl	71.77	99.85
	GL-12	Stb1	0.20	0.03	bdl	bdl	27.84	bdl	bdl	bdl	71.77	99.84
	GL-12	Stb1	0.20	bdl	0.04	bdl	27.82	bdl	0.03	bdl	71.76	99.87
	GL-12	Stb1	0.21	bdl	0.03	0.04	27.81	bdl	bdl	bdl	71.73	99.82
	GL-12	Stb1	0.22	bdl	bdl	bdl	27.80	bdl	0.07	bdl	71.73	99.82
	GL-12	Stb1	0.22	0.02	bdl	0.02	27.80	bdl	bdl	bdl	71.72	99.78
	GL-12	Stb1	0.22	0.02	0.03	0.03	27.79	bdl	0.05	bdl	71.64	99.76
	GL-12	Stb1	0.22	bdl	bdl	bdl	27.78	bdl	0.07	bdl	71.60	99.67
Euhedral-subhedral stibnite	LBC-5	Stb1	0.23	bdl	0.03	bdl	27.78	bdl	bdl	bdl	71.54	99.58
	LBC-5	Stb1	0.24	bdl	0.03	bdl	27.74	bdl	0.03	bdl	71.50	99.54
	LBC-5	Stb1	0.24	bdl	0.03	bdl	27.72	bdl	0.01	bdl	71.45	99.44
	LBC-5	Stb1	0.29	bdl	bdl	0.03	27.72	bdl	bdl	bdl	71.43	99.47
	LBC-5	Stb1	0.29	bdl	bdl	0.03	27.67	bdl	bdl	bdl	71.38	99.38
	LBC-5	Stb1	0.30	0.06	bdl	bdl	27.54	bdl	bdl	bdl	71.31	99.20
Fine-grained stibnite coexists with pyrite in Qtz	DSY6-4	Stb2	0.96	bdl	bdl	bdl	27.97	bdl	bdl	bdl	71.78	100.71
	DSY6-4	Stb2	0.91	bdl	0.02	bdl	27.99	bdl	bdl	bdl	71.35	100.28
	DSY6-4	Stb2	0.99	bdl	0.03	bdl	28.14	bdl	bdl	0.02	71.69	100.86
	DSY6-4	Stb2	0.99	0.02	bdl	0.04	27.92	bdl	bdl	bdl	71.76	100.72
	DSY6-4	Stb2	1.00	bdl	bdl	bdl	28.05	0.03	bdl	bdl	72.19	101.27
	DSY6-4	Stb2	1.08	0.04	bdl	0.05	27.95	bdl	bdl	bdl	71.70	100.83
	DSY6-5	Stb2	1.09	bdl	0.02	bdl	27.97	0.09	bdl	bdl	72.00	101.16
	DSY6-5	Stb2	1.12	0.04	0.03	bdl	28.24	bdl	bdl	bdl	71.83	101.25
	DSY6-5	Stb2	1.16	bdl	bdl	bdl	27.99	bdl	bdl	0.03	72.05	101.22
	DSY6-5	Stb2	1.20	0.02	bdl	0.03	27.98	bdl	bdl	bdl	71.32	100.55

Note: bdl = below the detection limit.

mineral assemblage at Qinglong (i.e., pyrite and stibnite, but no sulfates) suggests a medium to low temperature (161–294 °C), low fO_2, and acidic to neutral H_2S-dominated fluid condition (Chen et al., 2018). Under such condition, temperature has major effect on the H_2S $\delta^{34}S$ values, which can represent the ore-fluid $\delta^{34}S$ values (Ohmoto, 1972; Ohmoto and Rye, 1979). Using the equilibrium isotopic fractionation factors of stibnite-H_2S (1000 lnα(Sb_2S_3–H_2S) = −0.75 × 10^6/T^2) and pyrite-H_2S (1000 lnα(FeS_2–H_2S) = 0.40 × 10^6/T^2) (Ohmoto and Rye, 1979) and the early-ore (220 °C) and late-ore (175 °C) temperatures (average homogenization temperature of fluid inclusions in Stb1 and Stb2, respectively; Chen et al., 2018), we calculate the ore-fluid δS_{H_2S} values of Stb1 (−1.6‰ to +3.4‰, mean + 0.8‰, n = 17), Stb2 (−2.9‰ to +6.9‰, mean + 1.8‰, n = 17), and pyrite As-rich zones (−8.9‰ to +4.1‰, mean −3.1‰, n = 33).

The narrow $\delta^{34}S$ range (−5‰ to +5‰) precludes the possibility that the sulfur is from sedimentary rocks, but points to a magmatic or deep-metamorphic source (Ohmoto and Rye, 1979; Labidi et al., 2013; Xie et al., 2018; Li et al., 2020b). Despite that there are no exposed granitoids at Qinglong, felsic dykes were reported in some Carlin-style Au occurrences around it (Fig. 2; Su et al., 2018). Previous studies provided some evidence for the relations between the Sb and Au mineralization and felsic dikes: (1) Ore formation of the Carlin-like Au deposits (peak at 140 Ma; Chen et al., 2019; Zheng et al., 2019) and Qinglong Sb deposit (fluorite Sm-Nd isochron age: 148–142 Ma; Peng et al., 2003) are coeval with the emplacement of these felsic dikes (zircon U–Pb age: 140–100 Ma; Zhu et al., 2016, 2017); (2) Aeromagnetic surveys reveal concealed plutons beneath the Youjiang basin (Wang et al., 2009, 2015); (3) Stibnite He and Ar isotope data indicate that the Qinglong ore-forming fluids

are the mixture between a crustal fluid (with atmospheric Ar and crustal ^4He) and a fluid with mantle input (Chen et al., 2016); (4) The $\delta^{18}O_{VSMOW}$ values of hydrothermal zircon form Carlin-like deposits in Youjiang basin also show that the ore-forming fluids have had a magmatic origin (Zhu et al., 2020). Thus, we suggest that concealed plutons, if present, may have contributed some sulfur for the Au–Sb mineralization, although more work is needed to confirm that.

Compared to these hydrothermal Au–Sb sulfides, ore-barren pyrite As-poor/-free zones of our Qinglong samples have higher and more-varied $\delta^{34}S$ values (−18.9‰ to +18.1‰, mostly +3‰ to +12‰) (Fig. 12). These pyrite As-poor/-free zones are commonly porous, with lower Co/Ni ratios and some organic matter (Fig. 7A), and are thus interpreted to have a diagenetic/sedimentary origin (Bralia et al., 1979). The broad S-isotope range of the diagenetic/sedimentary pyrites in the Youjiang basin is likely the result of bacterial sulfate reduction (BSR) from marine sulfates during the Upper Permian sedimentation and diagenesis in (semi-) open and sulfate-limited systems (Xia, 2005; Hou et al., 2016; Xie et al., 2018b;Liu et al., 20120b).

5.3. Sulfur isotope comparison of Carlin-like Au deposits

In the NWYB, the texture, paragenesis and mineral chemistry of ore sulfides from the Carlin-like Au–Sb deposits have been described in detail by many previous studies (Su et al., 2008, 2009a,b, 2012, 2018; Tan et al., 2015; Hou et al., 2016; Chen et al., 2018; Hu et al., 2018a,b; Li et al., 2020b). All of these studies agreed that the Au and As are mainly concentrated in the hydrothermal rim of the ore-stage zoned pyrite (Appendix I), very similar to our case of Qinglong. The *in-situ* sulfur

Table 3
$\delta^{34}S_{V\text{-CDT}}$ values of Au-bearing pyrites and relative concentrations of As by in-situ NanoSIMS from the Qinglong Sb(Au) deposit.

Sample types	Pyrite	Spot	$\delta^{34}S_{CDT}$ (‰)	±SE	As-rich	As-poor	As-free
Coarse-grained and core-rim textured pyrites	Py3	dc5-q2_s1_mg_1	7.5	0.2			As-free
		dc5-q2_s1_mg_2	3.1	0.2			As-free
		dc5-q2_s1_mg_3	−1.4	0.2	As-rich		
		dc5-q2_s1_mg_4	7.0	0.3		As-poor	
	Py3	dc5-q2-s2_mg_1	−1.7	0.2	As-rich		
		dc5-q2-s2_mg_2	6.8	0.2		As-poor	
		dc5-q2-s2_mg_3	4.5	0.2			As-free
	Py2	dc5-q2-s3_mg_1	−1.5	0.3	As-rich		
		dc5-q2-s3_mg_2	**0.5**	0.3	As-rich		
		dc5-q2-s3_mg_3	1.8	0.3		As-poor	
	Py2	dc5-q2-s4_mg_1	**−2.8**	0.2	As-rich		
		dc5-q2-s4_mg_2	**1.6**	0.3	As-rich		
		dc5-q2-s4_mg_3	**−6.9**	0.3	As-rich		
		dc5-q2-s4_mg_4	3.7	0.2			As-free
		dc5-q2-s4_mg_5	12.0	0.3		As-poor	
	Py1	dc5-q2-s5_mg_1	−18.9	0.3			As-free
		dc5-q2-s5_mg_2	−18.5	0.2			As-free
Colloform pyrites	Py3	dc5-q2-s6_mg_1	4.5	0.2			As-free
		dc5-q2-s6_mg_2	−7.9	0.2			As-free
		dc5-q2-s6_mg_3	**0.3**	0.3		As-poor	
Fine-grained and core-rim textured pyrites	Py2	dc5-q2-s7_mg_1	−9.2	0.2	As-rich		
		dc5-q2-s7_mg_2	**−6.3**	0.2	As-rich		
		dc5-q2-s7_mg_3	**−3.4**	0.2	As-rich		
		dc5-q2-s7_mg_4	−5.1	0.3	As-rich		
		dc5-q2-s7_mg_5	−0.4	0.2	As-rich		
	Py2	dc5-q2-s8_mg_1	−2.5	0.3	As-rich		
		dc5-q2-s8_mg_2	−0.2	0.3	As-rich		
		dc5-q2-s8_mg_3	**1.4**	0.3	As-rich		
	Py3	dc5-q2-s9_mg_1	2.7	0.2			As-free
		dc5-q2-s9_mg_2	4.5	0.3			As-free
		dc5-q2-s9_mg_3	**1.6**	0.3	As-rich		
		dc5-q2-s9_mg_4	**1.5**	0.3	As-rich		
	Py3	dc5-q2-s10_mg_1	−4.8	0.5		As-poor	
		dc5-q2-s10_mg_2	**3.0**	0.4	As-rich		
		dc5-q2-s10_mg_3	**2.9**	0.3	As-rich		
Fine-grained pyrites in quartz veins	Py1	dc5-q2-s11_mg_1	**−2.1**	0.3	As-rich		
		dc5-q2-s11_mg_2	11.2	0.2			As-free
		dc5-q2-s11_mg_3	9.5	0.2			As-free
	Py1	dc5-q2-s12_mg_1	10.4	0.2		As-poor	
	Py2	dc5-q2-s12_mg_2	12.3	0.2		As-poor	
	Py2	dc5-q2-s13_mg_1	**−5.3**	0.2	As-rich		
		dc5-q2-s13_mg_2	**−4.3**	0.2	As-rich		
		dc5-q2-s13_mg_3	**−2.6**	0.2	As-rich		
	Py3	dc5-q2-s14_mg_1	−4.2	0.3			As-free
		dc5-q2-s14_mg_2	**−4.1**	0.2	As-rich		
	Py3	dc5-q2-s15_mg_1	−5.9	0.2	As-rich		
		dc5-q2-s15_mg_2	**−3.9**	0.2	As-rich		
Coarse-grained pyrites in quartz veins	Py3	4036-S16_mg_1	4.0	0.2		As-poor	
		4036-S16_mg_2	4.4	0.2		As-poor	
		4036-S16_mg_3	**3.0**	0.4	As-rich		
	Py3	4036-S17_mg_1	6.7	0.2		As-poor	
		4036-S17_mg_2	6.5	0.2			As-free
		4036-S17_mg_3	**3.5**	0.3	As-rich		
	Py2	4036-S18_mg_1	6.5	0.2			As-free
		4036-S18_mg_2	6.2	0.2			As-free
		4036-S18_mg_3	**3.7**	0.2	As-rich		
	Py2	4036-S19_mg_1	8.4	0.2		As-poor	
		4036-S19_mg_2	10.1	0.3			As-free
		4036-S19_mg_3	**6.8**	0.9			As-free
Fine-grained framboidal pyrite grains coexist with minor organic matter	Py1	4036-S20_mg_1	11.6	0.2		As-poor	
		4036-S20_mg_2	12.4	0.2		As-poor	
		4036-S20_mg_3	10.9	0.2		As-poor	
	Py2	4036-S21_mg_1	11.5	0.3		As-poor	
		4036-S21_mg_2	10.8	0.2			As-free
		4036-S21_mg_3	**6.1**	0.3	As-rich		
		4036-S21_mg_4	**5.6**	0.9	As-rich		
	Py1	4035-S22_mg_1	18.1	0.3			As-free
		4035-S22_mg_2	15.3	0.2		As-poor	
		4035-S22_mg_3	13.4	0.2		As-poor	
		4035-S22_mg_4	9.2	0.3		As-poor	
		4035-S22_mg_5	11.8	0.3		As-poor	

Note: On the basis of Au–As variations of NanoSIMS mapping, zoning is sharply defined and is clearly visible as alternating broad zones of varying colors, showing the presence of As-rich, As-poor and As-free zones in the Au-bearing pyrite.

isotope data (SHRIMP, LA-MC-ICP-MS and NanoSIMS) reveal that the Au–As-rich zones of the early-ore pyrites have a relatively narrow δ^{34}S range (−2.8‰ to +8.4‰; Fig. 13B). In addition, the δ^{34}S values of other late-ore sulfides (i.e., arsenopyrite, realgar, orpiment, and stibnite) have also a similarly narrow range (−4.9‰ to +5.3‰) (Appendix I; Fig. 13B).

Published fluid inclusion data of Carlin-like Au deposits in the NWYB (Su et al., 2009b, 2018; Chen et al., 2018) suggest that the early-ore and late-ore fluid inclusions homogenized at 190–278 °C (mean 210 °C) and 151–261 °C (mean 190 °C), respectively. Based on the fractionation

factors between aqueous sulfur and sulfides (Ohmoto and Rye, 1979), we calculated the isotope composition of H$_2$S in equilibrium with sulfides for the Carlin-like Au deposits in the NWYB (Appendix I), i.e., early-ore δS_{H_2S} (−4.5‰ to +6.7‰, mean −0.6‰ ± 2.4‰) and late-ore δS_{H_2S} (−1.4‰ to +8.5‰, mean 3.1‰ ± 3.9‰). Ore-fluid δS_{H_2S} values of the Au and Sb deposits in the NWYB are fairly similar (mostly −5‰ to +5‰) (Fig. 15), and points to a probable magmatic sulfur source (0 ± 5‰; Ohmoto and Rye, 1979; Labidi et al., 2013). Furthermore, fluid inclusions from Carlin-like deposits in the Youjiang basin contain significant amount of
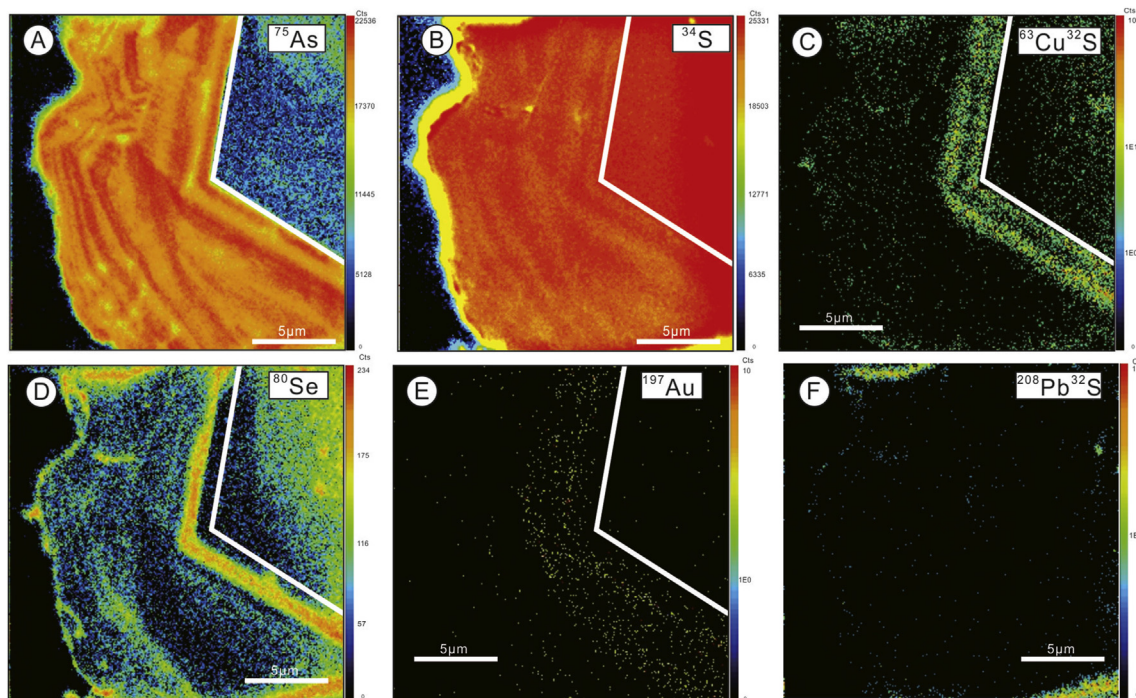
Fig. 10. NanoSIMS elemental maps of (A) ^{75}As, (B) ^{34}S, (C) ^{63}Cu^{32}S, (D) ^{80}Se, (E) ^{197}Au and (F) ^{208}Pb^{32}S for representative Au-bearing pyrite grains from Qinglong. Figures A, B and E from Chen et al. (2018).
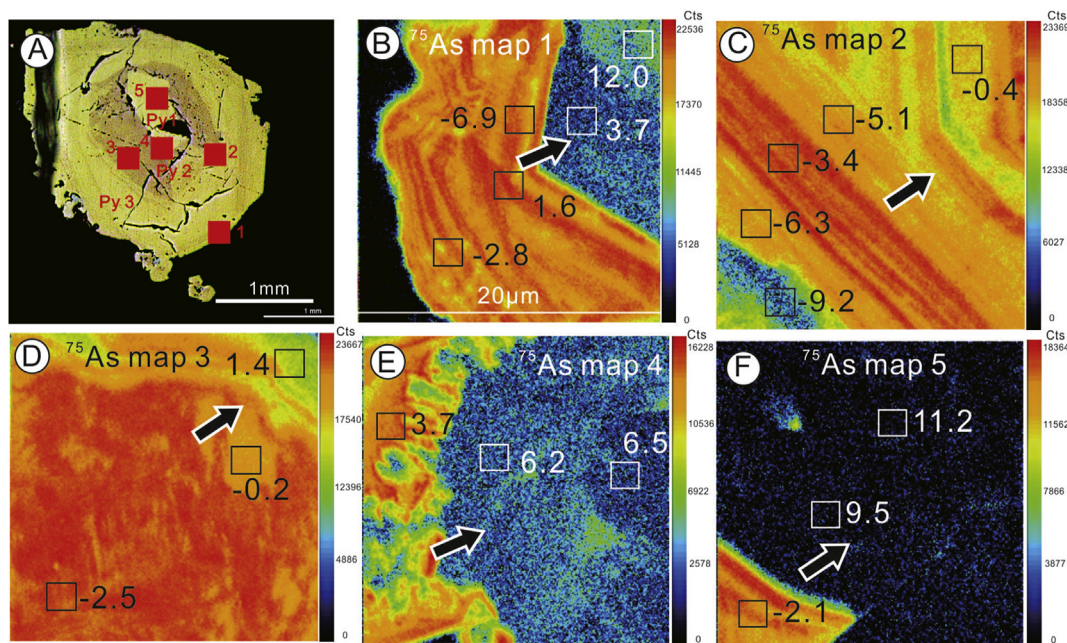

Fig. 11. Nanoscale-distribution of ^{75}As and variation of δ^{34}S values of representative Au-bearing pyrite from Qinglong. (A) Location of ablated spots (red squares) of Au-bearing pyrite; (B–F) Arsenic elemental maps of different ablated spots (size: 20 μm × 20 μm). Black arrow points to the core of zoned pyrite.
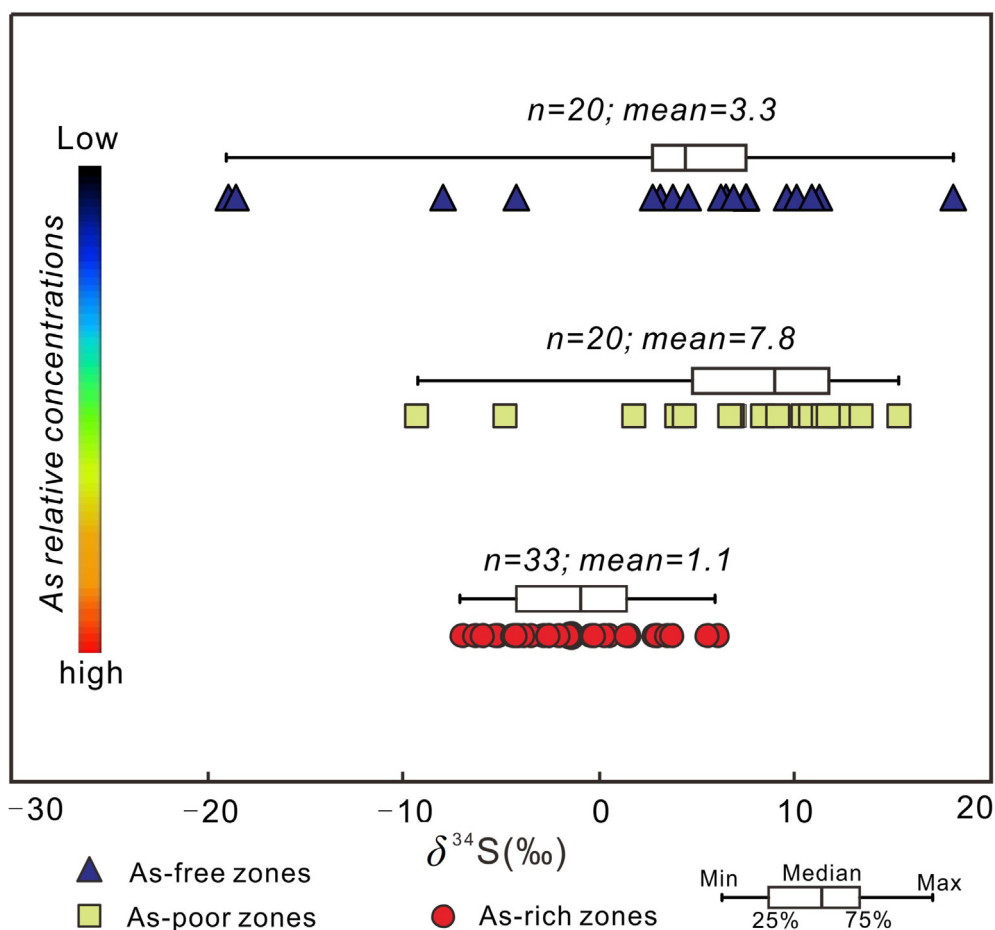
Fig. 12. Diagram showing the $\delta^{34}S_{V-CDT}$ values of the As-rich, As-poor and As-free zones in the zoned pyrite form Qinglong, showing that the As-rich zone has lower and narrower-range $\delta^{34}S_{V-CDT}$ (0 ± 5%).

CO_2 (>6 mol% for Yata deposit), and were estimated to have formed at ca. 4–6 km at depth (Su et al., 2009a). This is consistent with the emplacement depth of the felsic pluton as revealed from geophysical investigations. Published H–O isotope compositions of the ore-related quartz from Carlin-like deposits (Su et al., 2018; Li et al., 2020a) indicate that the ore fluids were formed in a magmatic-hydrothermal system with meteoric water incursion. Therefore, we infer that the Au-rich and Sb-rich ore fluids were derived from magmatic-related sources in the NWYB.

5.4. Variations of S isotopes and As concentrations as indicators for fluid evolution

Increasingly more studies have shown that microscale (intra-grain) sulfur isotopic variations in Au-bearing pyrites can provide constraints on the mineralization processes (Barker et al., 2009; Yan et al., 2018; Li et al., 2020b). As demonstrated in the sections above, the geochemical coupling of Au and As in pyrite is ubiquitous in many gold deposits. In this study, we compared the variation of As contents and $\delta^{34}S$ values in the Qinglong Py2 and Py3, reflecting sulfur isotopic fractionation during the ore-forming process. As shown in Fig. 14, the pyrite $\delta^{34}S$ value and range decrease gradually with increasing As content. In the hydrothermal stage (Py2 and Py3), the $\delta^{34}S$ range in the As-rich zone (−6.9‰ to 6.1‰) is narrower than in the As-poor zone (−9.2‰ to 15.3‰), indicating that the degree of sulfur isotopic fractionation also decreases with increasing As content.

Factors affecting the sulfur isotope signature of hydrothermal sulfides include the fluid T, pH, and fO_2, as well as the $\delta^{34}S$ values of the H_2S that precipitates the sulfide phases. As above-mentioned, the wide fluid-temperature range (161–294 °C; Chen et al., 2018) at Qinglong has affected the δS_{H_2S} values, and the fractionation between H_2S and sulfides cannot be ignored (Ohmoto and Rye, 1979). For the Qinglong case, our calculated mineral-H_2S fractionation is 1.8‰ (pyrite-H_2S) and −3.4‰ (stibnite-H_2S) at 200 °C. Consequently, temperature is likely less important in producing the observed $\delta^{34}S$ variations, because the sulfur isotope fractionation between H_2S and pyrite/stibnite are <6‰ under such low-temperature condition (161–294 °C). In addition, there is little evidence that pyrite and barite coexist at Qinglong, even though the Ba contents of pyrites (from LA-ICP-MS) can be up to 1560 ppm (Table 1). Ohmoto (1972) suggested that the changes in pH and fO_2 can only slightly affect the sulfide $\delta^{34}S$ variations in sulfate-poor/-free systems, thus the observed $\delta^{34}S$ variation may have controlled largely by the $\delta^{34}S_{H_2S}$ during sulfide deposition.

The Qinglong pyrite core has an elevated $^{34}S/^{32}S$ ratios (mostly 3‰– 12‰) with lower Co/Ni ratios (mean 0.31) and ore-element (As, Au and Sb) concentrations, suggesting that the pyrite core was formed through sulfate-limited BSR process (Ohmoto, 1972). However, magmatic-hydrothermal fluids are commonly featured by minor isotope fractionation (<10‰) and near-zero $\delta^{34}S$ values (Ohmoto and Rye, 1979; Labidi et al., 2013). NanoSIMS mapping and $\delta^{34}S$ variation indicate that the pyrite rim with the highest Au–As contents was formed through ongoing interactions between the magmatic fluid (evidenced from our S isotope data) and sedimentary pyrites (preserved in the pyrite core). The textural features (fuzzy, wavy, irregular) of the auriferous pyrite core-rim contacts (Figs. 7E, F and 9) also indicate that the formation of Au–As-rich rims by reacting the pyrite core with ore fluids. Such dissolution and reprecipitation replacement of auriferous pyrite is ubiquitous in hypogene gold mineralization systems worldwide (e.g., Morey et al., 2008;

Table 4
The $\delta^{34}S_{V-CDT}$ values of stibnite from the Qinglong Sb(Au) deposit.

Stages	$\delta^{34}S_{V-CDT}$ (‰)	δS_{H_2S} (‰)	References
Stibnite 1	−1.3	1.8	This paper
Stibnite 1	−1.3	1.8	
Stibnite 1	−1.1	2.0	
Stibnite 1	−1.0	2.1	
Stibnite 1	−0.6	2.5	
Stibnite 1	0.3	3.4	
Stibnite 1	−3.9	−0.8	Chen et al. (2018)
Stibnite 1	−2.7	0.4	
Stibnite 1	−4.1	−1.0	
Stibnite 1	−2.2	0.9	
Stibnite 1	−2.8	0.3	
Stibnite 1	−1.4	1.7	
Stibnite 1	−4.3	−1.2	
Stibnite 1	−1.7	1.4	
Stibnite 1	−4.5	−1.4	
Stibnite 1	−4.7	−1.6	
Stibnite 1	−0.9	2.2	
Stibnite 2	0.4	4.1	This paper
Stibnite 2	0.4	4.1	
Stibnite 2	2.4	6.1	
Stibnite 2	3.2	6.9	
Stibnite 2	2.6	6.3	
Stibnite 2	−6.2	−2.5	Chen et al. (2018)
Stibnite 2	−1.5	2.2	
Stibnite 2	−6.6	−2.9	
Stibnite 2	−4.4	−0.7	
Stibnite 2	−2.4	1.3	
Stibnite 2	−3.6	0.1	
Stibnite 2	−2.5	1.2	
Stibnite 2	−1.5	2.2	
Stibnite 2	−3.8	−0.1	
Stibnite 2	−3.1	0.6	
Stibnite 2	−4.3	−0.6	
Stibnite 2	−2.5	1.2	

Note: The sulfur isotope data of this paper were performed by fs-LA-MC-ICP-MS. The data of Chen et al. (2018) are based on bulk mineral analysis.

Fig. 13. $\delta^{34}S_{V-CDT}$ histogram of hydrothermal ore minerals from Qinglong (A) and other Carlin-like gold deposits (B) in the northwestern margin of the Youjiang basin. Data of the pyrite As-rich zones are from Hou et al. (2016), Hu et al. (2018a,b) and this paper, which are obtained by SHRIMP, LA-MC-ICP-MS and NanoSIMS, respectively. Stibnite, Realgar and orpiment bulk-mineral data are from Xia (2005) and Chen et al. (2018).

Wu et al., 2019).

During the hydrothermal stage, the pyrite core was dissolved by the gold-bearing fluids, providing an iron source for the subsequent arsenian pyrite precipitation along the pre-existing pyrite margins (Holley et al., 2019). The reaction-induced porosity in pyrite core suggests that the parent pyrite replacement may have proceeded via a dissolution and reprecipitation mechanism (Simon et al., 1999; Wu et al., 2019). The reaction rim of pyrites commonly contains multiple As-rich and As-poor bands (Fig. 11B and C), and the $\delta^{34}S$ values decrease gradually with increasing As concentrations (Fig. 14). The alternating $\delta^{34}S$ and As variation appears to reflect ore-fluid chemical fluctuations, and suggests episodic incursion of magmatic-related fluids. The available information indicates that the fluids likely contained sufficient H_2S to transport gold in bisulfide complexes in Carlin-type hydrothermal system (Xie et al., 2018b; Holley et al., 2019). The observed $\delta^{34}S$ variation at Qinglong may have been controlled mainly by the δS_{H_2S} composition during sulfide deposition. More significant $\delta^{34}S$ increase can be resulted from changes in the proportion of oxidized and reduced sulfur species in the fluids (Rye and Ohmoto, 1974). In magmatic-hydrothermal system, the relative proportion of SO_2 and H_2S is controlled by the fluid/rock ratio (Giggenbach, 1987). When the pre-existing pyrite interacted with magmatic-hydrothermal fluids, both the H_2S to SO_2 ratios (Holley et al., 2019) and As contents increase at the reaction rim (Xing et al., 2019), as shown in As-rich Py2 (Fig. 9), which also results in gold incorporation. Accordingly, as the magmatic-hydrothermal fluid (with high As and low $\delta^{34}S$) incursion has episodically increased the H_2S/SO_2 ratio over time, the $\delta^{34}S$ values progressively decrease with increasing As, reaching −5‰ to +5‰. Such variation of the trace elements and S isotopes is also reported by Barker et al. (2009) and Gopon et al. (2019), demonstrating that higher trace element concentrations are associated with lower $^{34}S/^{32}S$ ratios.

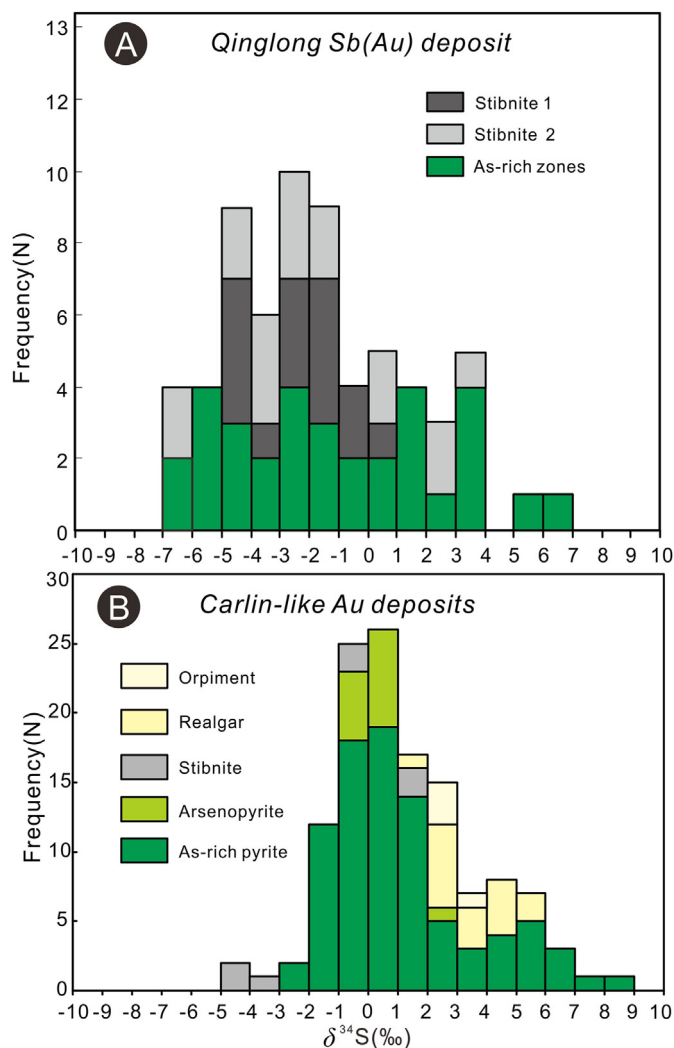## 5.5. Precipitation of stibnite and arsenian pyrite

This study has shown that the gold and antimony deposits in the NWYB have some geological similarities but also significant differences. Comparison between the Shuiyindong and Nibao Carlin-like gold deposit and the Qinglong Sb(Au) deposit is summarized in Table 5.

These similarities include similar mineralization ages (ca. ~140 Ma), ore-related alteration styles, ore mineral assemblages, ore host and possibly a magmatic-related ore-fluid source (Table 5; Su et al., 2008, 2009a, b, 2012, 2018; Cline et al., 2013; Hou et al., 2016; Chen et al., 2018). However, a key difference between the gold and antimony deposits occurs in the nature of ore fluids. At Qinglong, Sb ores were formed in early-ore stage, Chen et al. (2018) estimated that the Sb-rich ore fluids in this stage are medium to low temperatures (161–294 °C, mean 220 °C), with wide salinity range (0.35–13.18 wt% NaCl eqv.) and acidic. Whereas for the Shuiyidong Au-rich ore fluids, although the temperatures are similarly medium to low (190–250 °C, mean 210 °C), the salinity is considerably lower and narrower-range (4.2–6.9 wt% NaCl eqv.), less acidic, and with higher CO_2 concentration (6–8 mol%) (Su et al., 2009a). Fluid inclusion studies in Qinglong indicate that the major temperature and fO_2 drop may have reduced the Sb solubility and
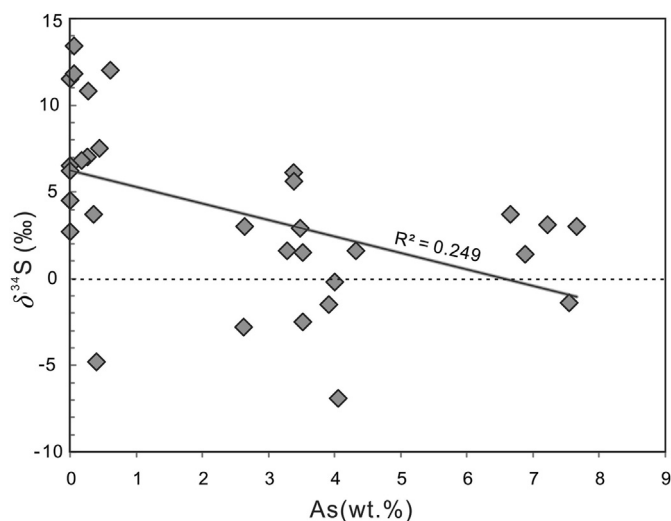
Fig. 14. δ^{34}S vs. As diagram (EPMA arsenic data collected on the same spots as the NanoSIMS S-isotope analysis), showing pyrite δ^{34}S value and range decrease gradually with increasing As contents.

triggered abundant stibnite precipitation (Chen et al., 2018). At Shuiyindong, gold-bearing arsenian pyrite precipitated from H_2S-rich fluids by sulfidation of the ore host, and/or mixing with Fe-rich fluids produced by ferroan mineral dissolution in the alteration zones nearby (Su et al., 2009b, 2018). Therefore, Au-rich and Sb-rich fluids were probably formed via fluid homogenization by chemical re-equilibrium and/or fluid-mixing at depth. This is supported by that ore-related elements (notably As, Sb, and Au) are enriched in fluid inclusions in the Shuiyindong ore-related quartz (Su et al., 2009a). The decreasing δ^{34}S value with increasing As concentrations (Fig. 14) in pyrite grains may reflect Au ore formation via episodic incursion of low-δ^{34}S, magmatic-related auriferous fluids.

Auriferous arsenian pyrite coexists with stibnite (Stb2) occur in late-stage quartz (Fig. 7C) at Qinglong. It is worth noting that Stb2 has higher As (0.91–1.20 wt.%; Fig. 8F) than Stb1. Indeed, the role of As (in melt) in producing micropits (defect sites) has also been demonstrated by experiment (Pruseth and Sahu, 2017). In the hydrothermal regime in which such arsenian pyrite was formed, Au–Sb and As_2S_3–Sb_2S_3 melts are stable (Okamoto and Massalski, 1984; Tomkins et al., 2004). In the temperature range (<300 °C) of interest here, sulfide melts may coexist with hydrothermal fluid. The fractional crystallization of sulfide melt in melt-aqueous fluid system during prograde metamorphism has been documented elsewhere by Hofmann (1994). The eutectic between As_2S_3 and Sb_2S_3 is at ~250 °C, or even lower with the presence of Cu, Ag and H_2O. Based on the temperature of fluid inclusions in Stb2 (mean 220 °C; Chen et al., 2018) and positive As vs. Au–Sb–Cu–Ag correlations (Figs. 8 and 9), we propose that the As_2S_3–Sb_2S_3 melt could be present in Au–Sb-rich ore fluids under such conditions. As the ore fluid comes into contact with pre-existing pyrite, stibnite and arsenian pyrite could be an equilibrium assemblage from the As_2S_3–Sb_2S_3 melt separate (Pruseth and Sahu, 2017). Meanwhile, pre-existing pyrite likely became extremely porous, which is consistent with the observed the porous pyrite core (Fig. 7E and F).

5.6. Genetic model for the NWYB gold and antimony deposits

Based on the discussion above, we propose a new metal transport and deposition model for the gold and antimony mineralization in the NWYB (Fig. 16). In the late Yanshanian period (~140 Ma), high-temperature magmatic-hydrothermal fluids may have ascended along extensional basinal faults across the deformed sedimentary sequences (Wang and Groves, 2018 and references therein), and leached ore-forming elements (e.g., Au, Sb, and As) from the basement rocks (e.g., Lower Cambrian Niutitang Fm. black shale with abundant anomalies of these elements; Zhang et al., 2016). When the S–As–Au–Sb-rich ore fluids ascended to 1.7–4.3 km under lithostatic pressure (Su et al., 2018), fluid boiling may have occurred due to the sharp pressure drop (e.g., at Taipingdong deposit; Liu et al., 2012), and led to fluid immiscibility that formed two discrete ore fluids (Fig. 16). These two fluids are, namely, an Au–As-rich,
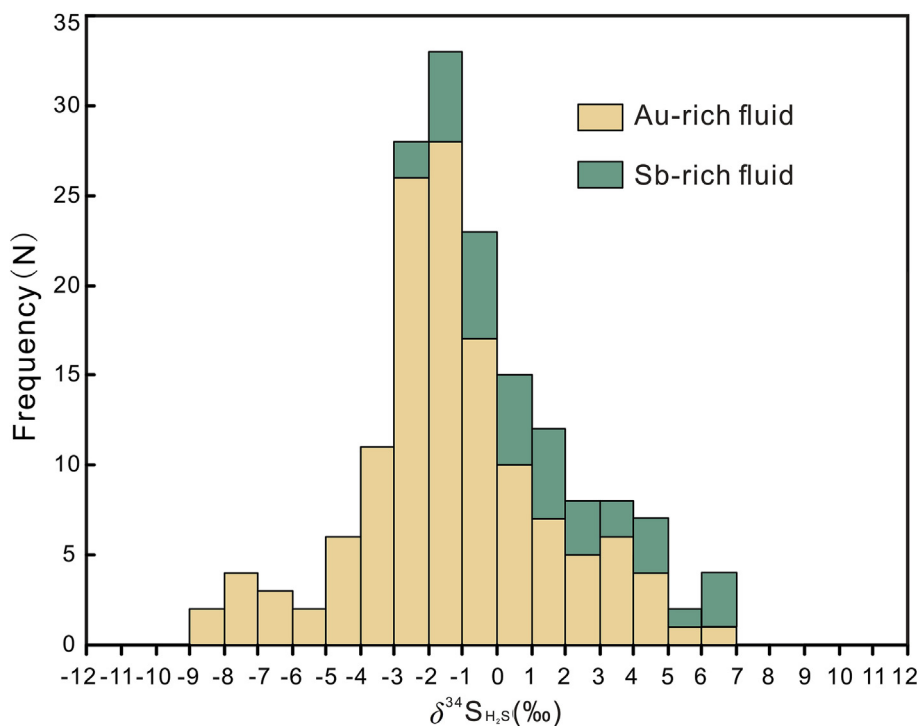

Fig. 15. δS_{H_2S} histogram of Au- and Sb-rich ore fluids in the NWYB. Extensive precipitation of Au-bearing pyrite (for Carlin-like Au deposits) and stibnite (for Sb deposit such as Qinglong) were likely precipitated in the early-ore stage. 90% of the δS_{H_2S} data fall between −5.0‰ and +5.0‰.

Table 5
Comparison of representative gold deposit and antimony deposit in the northwestern margin the Youjiang basin.

Representative deposits	Gold deposit		Antimony deposit	
	Nibao and Shuiyindong		Qinglong	
Age	~140 Ma		142–148 Ma	
Host rock	Permian carbonate		Permian carbonate/siltstone	
Mineralization type	Au mineralization	Sb mineralization	Au mineralization	Sb mineralization
Sequence	**Early-ore stage**	**Late-ore stage**	**Late-ore stage**	**Early-ore stage**
Ore-related alterations	Decarbonatization, silicifcation, sulfdation, and dolomitization	Calcitization	Silicifcation, sulfdation and illitization	Silicifcation and kaolinization
Ore minerals	Arsenian pyrite and aesenopyrite	Stibnite, orpiment and realgar	Arsenian pyrite and stibnite	Stibnite
Gangue minerals	Quartz and dolomite	Calcite and Quartz	Quartz	Quartz and fluorite
Temperature (°C)	190–278 (av. 210)	151–261 (av. 190)	113–255 (av. 175)	161–294 (av. 220)
Salinity (wt.% NaCl equiv)	4.2–6.9	0.2–7.2	0.0–6.3	0.4–13.2
Volatile phases	CO_2-rich	–	–	Hydrocarbon
pH	Acidic to neutral	–	Faintly acidic to neutral	Acidic
$\delta^{34}S$ (‰)	−2.7 to 4.7	−4.9 to 6.2	−6.9 to 6.1	−4.7 to −0.9
Reference	Su et al. (2008, 2009a,b, 2012, 2018), Cline et al. (2013), Hou et al. (2016)		Chen et al. (2018), this paper	

medium salinity (~5 wt.% NaCl eqv.) and temperature (~210 °C), and varying CO_2 fluid that formed the gold deposits, and a Sb-rich, medium to low temperatures (161–294 °C), and varying salinities (0.4–13.2 wt.% NaCl eqv.) fluid that formed the antimony deposits such as Qinglong (Fig. 16). When these fluids percolated into the interlayer fracture zones in the Upper Permian carbonates, the substantial physicochemical changes (e.g., fluid composition, redox, temperature) may have triggered the Au and Sb ore deposition. For the case of Qinglong, the euhedral and coarse-grained stibnite in the early-stage (Fig. 4A) was formed in open-space polymictic breccias, whereas the late-stage quartz is inter-grown with fine-grained disseminated Au-bearing pyrite as veins/stockworks (Fig. 5C and D). The brecciated wallrocks likely allowed efficient fluid mixing and caused significant temperature and fO_2 drop, which reduced the stibnite solubility and triggered its precipitation. The

intact (non-brecciated) wallrock (Fig. 5D) may have had low porosity in the late-ore stage, which promoted intense fluid-rock interactions. The gold mineralization may be resulted from episodic influx of a gold-rich fluid that was partly derived from, or interacted with, pre-ore pyrite and wallrocks.

6. Conclusions

(i) The Qinglong Sb(Au) deposit is characterized by early-stage Sb mineralization and late-stage Sb–Au mineralization. Three generations of pyrite (Py1, Py2 and Py3) and two generations of stibnite (Stb1 and Stb2) are recognized.

(ii) Py1 is featured by its lower ore element (Au, As, Sb, Cu and Ag) contents and Co/Ni ratios (<1) than the ore-stage Py2 and Py3,
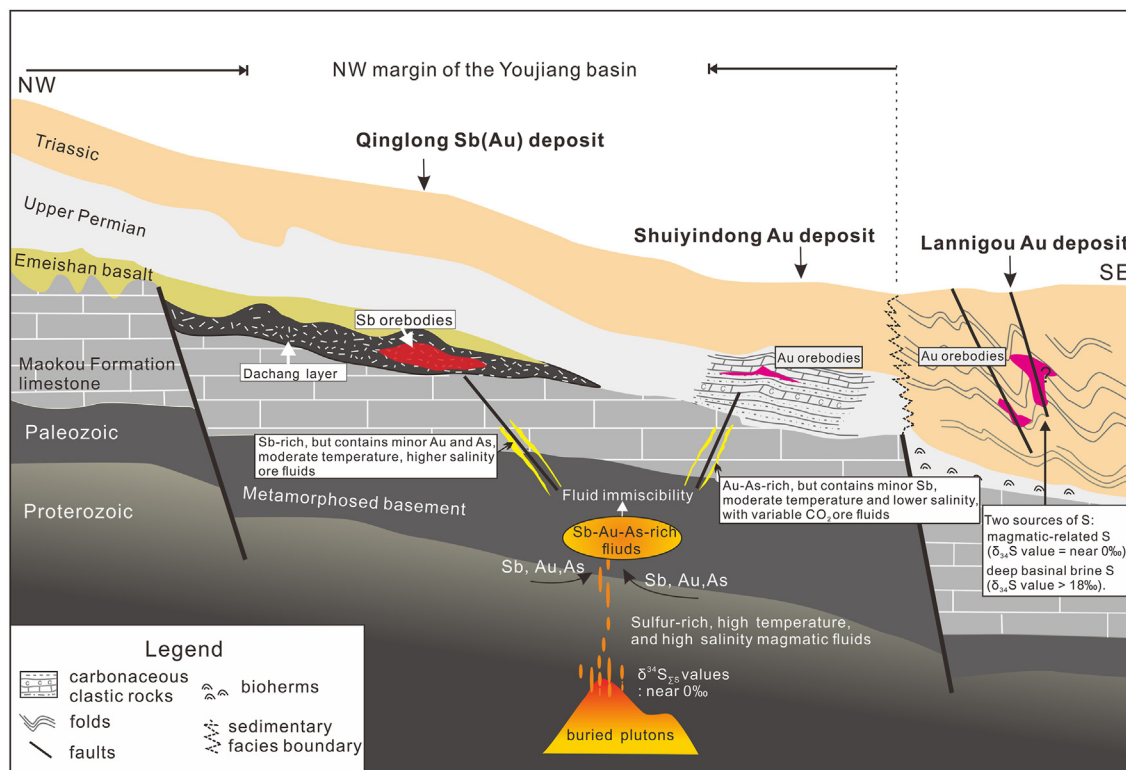

Fig. 16. Schematic metallogenic model for Au–Sb deposits in the NWYB, showing the separated evolution of Au- and Sb-rich ore fluids (modified from Chen et al., 2018).

indicating a syn-diagenetic origin for Py1 and a hydrothermal one for Py2 and Py3. Early-ore Stb1 has lower As than late-ore Stb2. The positive As vs. Au–As–Sb–Cu–Ag correlations show that the progressive As enrichment in pyrite is accompanied by the rising of other ore-forming elements (Au, Sb, Cu and Ag) when the fluid system evolved.

(iii) NanoSIMS sulfur isotope and element mapping suggest that the pyrite δ^{34}S value and range decrease gradually with increasing As content, implying that the pyrite was formed via episodic incursion of auriferous magmatic-related fluids. The ore fluid incursion has episodically increased the H_2S/SO_2 ratio via ongoing fluid/mineral interaction, causing the progressive δ^{34}S decrease with increasing As, which may have produced the alternating variation in the pyrite δ^{34}S and As content.

(iv) Comparing the Au and Sb deposits in the NWYB, we favor a magmatic-related source for the Au–Sb–As-rich ore fluids, but the Au-rich and Sb-rich ore fluids may have evolved at different stages of the ore-forming process.

Declaration of competing interest

The authors declare that they have no known competing financial interests or personal relationships that could have appeared to influence the work reported in this paper.

Acknowledgements

Appendix A. Supplementary data

Supplementary data to this article can be found online at https://doi.org/10.1016/j.gsf.2020.08.010.

References

Barker, S., Hickey, K.A., Cline, J.S., Dipple, G.M., Kilburn, M.R., Vaughan, J.R., Longo, A.A., 2009. Uncloaking invisible gold: use of NanoSIMS to evaluate gold, trace elements, and sulfur isotopes in pyrite from Carlin-type gold deposits. Econ. Geol. 104, 897–904.

Bralia, A., Sabatini, G., Troja, F., 1979. A revaluation of the Co/Ni ratio in pyrite as geochemical tool in ore genesis problems. Miner. Deposita 14, 353–374.

Chen, D.Y., 1992. The low-temperature geochemical characteristics of ore-forming fluid of the Dachang antimony deposit in Qinglong. Bull. China Soc. Mineral Petrol. Geochem. 11, 3–5 (in Chinese with English abstract).

Chen, J., Yang, R.D., Du, L.J., Zheng, L.L., Gao, J.B., Lai, C.K., Wei, H.R., Yuan, M.G., 2018. Mineralogy, geochemistry and fluid inclusions of the Qinglong Sb-(Au) deposit, Youjiang basin (Guizhou, SW China). Ore Geol. Rev. 92, 1–18.

Chen, M.H., Zhang, Z., Santosh, M., Dang, Y., Zhang, W., 2015. The Carlin-type gold deposits of the "golden triangle" of SW China: Pb and S isotopic constraints for the ore genesis. J. Asian Earth Sci. 103, 115–128.

Chen, M.H., Bagas, L., Liao, X., Zhang, Z.Q., Li, Q.L., 2019. Hydrothermal apatite SIMS Th-Pb dating: constraints on the timing of low-temperature hydrothermal Au deposits in Nibao, SW China. Lithos 324, 418–428.

Chen, X., Su, W.C., Huang, Y., 2016. He and Ar isotope geochemistry of ore-forming fluids for the Qinglong Sb deposit in Guizhou Province, China. Acta Petrol. Sin. 32, 3312–3320 (in Chinese with English abstract).

Chen, Y.J., Zhai, M.G., Jiang, S.Y., 2009. Significant achievements and open issues in study of orogenesis and metallogenesis surrounding the North China continent. Acta Petrol. Sin. 25, 2695–2726 (in Chinese with English abstract).

Cline, J.S., 2001. Timing of gold and arsenic sulfide mineral deposition at the Getchell Carlin-type gold deposit, north-central Nevada. Econ. Geol. Bull. Soc. Econ. Geol. 96, 75–89.

Cline, J.S., Hofstra, A.H., Muntean, J.L., Tosdal, R.M., Hickey, K.A., 2005. Carlin-type gold deposits in Nevada, USA: critical geologic characteristics and viable models. Econ. Geol. 100th Anniversary Volume 451–484.

Cline, J.S., Muntean, J.L., Gu, X.X., Xia, J., 2013. A comparison of Carlin-type gold deposits: Guizhou Province, golden triangle, Southwest China, and northern Nevada, USA. Earth Sci. Front. 20, 1–18 (in Chinese with English abstract).

Cook, N.J., Ciobanu, C.L., Mao, J.W., 2009. Textural control on gold distribution in as-free pyrite from the Dongping, Huangtuliang and Hougou gold deposits, north China craton (Hebei Province, China). Chem. Geol. 264, 101–121.

Deditius, A.P., Reich, M., Kesler, S.E., Utsunomiya, S., Chryssoulis, S.L., Walshe, J., Ewing, R.C., 2014. The coupled geochemistry of Au and as in pyrite from hydrothermal ore deposits: Geochim. Cosmochim. Acta 140, 644–670.

Farquhar, J., Cliff, J., Zerkle, A.L., Kamyshny, A., Poulton, S.W., Claire, M., Adams, D., Harms, B., 2013. Pathways for Neoarchean pyrite formation constrained by mass-independent sulfur isotopes. Proc. Natl. Acad. Sci. U.S.A. 110, 17638–17643.

Fleet, M.E., Mumin, A.H., 1997. Gold-bearing arsenian pyrite and marcasite and arsenopyrite from Carlin trend gold deposits and laboratory synthesis. Am. Mineral. 82, 182–193.

Giggenbach, W.F., 1987. Redox processes governing the chemistry of fumarolic gas discharges from White Island, New Zealand. Appl. Geochem. 2, 43–161.

Gopon, P., Douglas, J.O., Auger, M.A., Hansen, L., Wade, J., Cline, J.S., Robb, L.J., Moody, M.P., 2019. A Nanoscale investigation of carlin-type gold deposits: an atom-scale elemental and isotopic perspective. Econ. Geol. 114, 1123–1133.

Guizhou Bgmr Bureau of Geology and Mineral Resources, 1987. Regional Geology of Guizhou Province. Geol. Publ. House, Beijing, pp. 1–666 (in Chinese).

Hofmann, B.A., 1994. Formation of a sulfide melt during Alpine metamorphism of the Lengenbach polymetallic sulfide mineralization, Binntal, Switzerland. Miner. Deposita 29, 439–442.

Holley, E.A., Lowe, J.A., Johnson, G.A., Pribil, M.J., 2019. Magmatic-hydrothermal gold mineralization at the Lone Tree Mine, Battle Mountain District, Nevada. Econ. Geol. 114, 811–856.

Hou, L., Peng, H.J., Ding, J., Zhang, J.R., Zhu, S.B., Wu, S.Y., Wu, Y., Ouyang, H.G., 2016. Textures and in situ chemical and isotopic analyses of pyrite, Huijiabao Trend, Youjiang Basin, China: implications for paragenesis and source of sulfur. Econ. Geol. 111, 331–353.

Hu, R.Z., Fu, S.L., Huang, Y., Zhou, M.F., Fu, S.H., Zhao, C.H., Wang, Y.J., Bi, X.W., Xiao, J.F., 2017. The giant South China Mesozoic low-temperature metallogenic domain: reviews and a new geodynamic model. J. Asian Earth Sci. 137, 9–34.

Hu, R.Z., Su, W.C., Bi, X.W., Tu, G.Z., Hofstra, A.H., 2002. Geology and geochemistry of Carlin-type gold deposits in China. Miner. Deposita 37, 378–392.

Hu, R.Z., Zhou, M.F., 2012. Multiple Mesozoic mineralization events in South China—an introduction to the thematic issue. Miner. Deposita 47, 579–588.

Hu, X.L., Gong, Y.J., Zeng, G.P., Zhang, Z.J., Wang, J., Yao, S.Z., 2018a. Multistage pyrite in the Getang sediment-hosted disseminated gold deposit, southwestern Guizhou Province, China: insights from textures and in situ chemical and sulfur isotopic analyses. Ore Geol. Rev. 99, 1–16.

Hu, X.L., Zeng, G.P., Zhang, Z.J., Li, W.T., Liu, W.H., Gong, Y.Z., Yao, S.Z., 2018b. Gold mineralization associated with Emeishan basaltic rocks: mineralogical, geochemical, and isotopic evidences from the Lianhuashan ore field, southwestern Guizhou Province, China. Ore Geol. Rev. 95, 604–619.

Krupp, R.E., 1988. Solubility of stibnite in hydrogen sulfide solutions speciation and equilibrium constants from 25 to 350°C. Geochem. Cosmochim. Acta 52, 3005–3015.

Kusebauch, C., Gleeson, S.A., Oelze, M., 2019. Coupled partitioning of Au and as into pyrite controls formation of giant Au deposits. Sci. Adv. 5, 1–8.

Labidi, J., Cartigny, P., Moreira, M., 2013. Non-chondritic sulphur isotope composition of the terrestrial mantle. Nature 501, 208–211.

Large, R.R., Danyushevsky, L., Hollit, C., Maslennikov, V., Meffre, S., Gilbert, S., Bull, S., Scott, R., Emsbo, P., Thomas, H., Singh, B., Foster, J., 2009. Gold and trace element zonation in pyrite using a laser imaging technique: implications for the timing of gold in orogenic and Carlin-style sediment-hosted deposits. Econ. Geol. Bull. Soc. Econ. Geol. 104, 635–668.

Li, J.W., Hu, R.Z., Xiao, J.F., Zhuo, Y.Z., Yan, J., Oyebamiji, A., 2020a. Genesis of gold and antimony deposits in the Youjiang metallogenic province, SW China: evidence from in situ oxygen isotopic and trace element compositions of quartz. Ore Geol. Rev. 116, 103257. https://doi.org/10.1016/j.oregeorev.2019.103257.

Li, J.X., Hu, R.Z., Zhao, C.H., Zhu, J.J., Huang, Y., Gao, W., Li, J.W., Zhuo, Y.Z., 2020b. Sulfur isotope and trace element compositions of pyrite determined by NanoSIMS and LA-ICP-MS: new constraints on the genesis of the Shuiyindong Carlin-like gold deposit in SW China. Miner. Deposita 55, 1279–1298. https://doi.org/10.1007/s00126-019-00929-w.

Li, Y., Xu, W.Q., Liu, W.H., Li, H., Dai, P.G., 2005. Sulfur-lead isotope geochemistry of micro disseminated Au deposits in Yunnan-Guizhou-Guangxi area. Acta Geosci. Sin. S1, 168–170 (in Chinese with English abstract).

Liu, L., Gu, X.X., Peng, Y.W., Zhang, Y.M., Wu, C.Y., Cheng, W.B., 2012. Characteristics of fluid inclusions and fluid immiscibility mechanism of the Taipingdong gold deposit, Guizhou. Acta Petrol. Sin. 28, 1568–1576 (in Chinese with English abstract).

Liu, Y.S., Hu, Z.C., Gao, S., Günther, D., Xu, J., Gao, C.G., Chen, H.H., 2008. In situ analysis of major and trace elements of anhydrous minerals by LA-ICP-MS without applying an internal standard. Chem. Geol. 257, 34–43.

Liu, S., Su, W., Hu, R., Feng, C., Gao, S., Coulson, I.M., Wang, T., Feng, G., Tao, Y., Xia, Y., 2010. Geochronological and geochemical constraints on the petrogenesis of alkaline ultramafic dikes from southwest Guizhou Province, SW China. Lithos 114, 253–264.

Morey, A.A., Tomkins, A.G., Bierlein, F.P., Weinberg, R.F., Davidson, G.J., 2008. Bimodal distribution of gold in pyrite and arsenopyrite: examples from the archean boorara and bardoc shear systems, Yilgarn Craton, Western Australia. Econ. Geol. 103, 599–614.

Muntean, J.L., Cline, J.S., 2018. Diversity of Carlin-style gold deposits. Rev. Econ. Geol. 20, 1–6.

Ohmoto, H., 1972. Systematics of sulfur and carbon isotopes in hydrothermal ore deposits. Econ. Geol. 67, 551–578.

Ohmoto, H., Rye, R.O., 1979. Isotopes of sulfur and carbon. In: Barnes, H.L. (Ed.), Geochemistry of Hydrothermal Ore Deposits, second ed. Wiley, New York, pp. 509–567.

Okamoto, H., Massalski, T.B., 1984. The Au–Sb (Gold-Antimony) system. J. Phase Equil. 5, 166–171.

Peng, J.T., Hu, R.Z., Jiang, G.H., 2003. Samarium-Neodymium isotope system of fluorites from the Qinglong antimony deposit, Guizhou Province: constraints on the mineralizing age ore-forming materials' sources. Acta Petrol. Sin. 19, 785–791 (in Chinese with English abstract).

Peters, S.G., Huang, J.Z., Li, Z.P., Jing, C.G., 2007. Sedimentary rock-hosted Au deposits of the dian–qian–gui area, Guizhou, and yunnan provinces, and guangxi district, China. Ore Geol. Rev. 31, 170–204.

Pi, Q.H., Hu, R.Z., Xiong, B., Li, Q.L., Zhong, R.C., 2017. In situ SIMS U-Pb dating of hydrothermal rutile: reliable age for the Zhesang Carlin-type gold deposit in the golden triangle region, SW China. Mineral. Depos 52, 1179–1190.

Pruseth, K.L., Sahu, P., 2017. Pyrite nanoparticles: potential source of as in groundwater. In: Goldschmidt Conference 2017. Paris, France.

Qin, L.J., Liu, D.M., 2006. Geochemical characteristics of rocks and soil at the southeast limb of Xiongwu anticline and direction of Au deposits. Guizhou Geol. 23, 187–196 (in Chinese with English abstract).

Reich, M., Kesler, S.E., Utsunomiya, S., Palenik, C.S., Chryssoulis, S.L., Ewing, R.C., 2005. Solubility of gold in arsenian pyrite. Geochim. Cosmochim. Acta 69, 2781–2796.

Rye, R.O., Ohmoto, H., 1974. Sulfur and carbon isotopes and ore genesis: a review. Econ. Geol. 69, 826–842.

Seward, T.M., 1973. Thio complexes of gold and the transport of gold in hydrothermal ore solutions. Geochmim. Cosmochim. Acta 37, 379–399.

Simon, G., Kesler, S.E., Chryssoulis, S., 1999. Geochemistry and textures of gold-bearing arsenian pyrite, Twin Creeks, Nevada; implications for deposition of gold in Carlin-type deposits. Econ. Geol. 94, 405–421.

Spycher, N.F., Reed, M.H., 1989. As (III) and Sb (III) sulfide complexes: an evaluation of stoichiometry and stability from existing experimental data. Geochem. Cosmochim. Acta 53, 2185–2194.

Su, W.C., Dong, W.D., Zhang, X.C., Shen, N.P., Hu, R.Z., Hofstra, A.H., Cheng, L.Z., 2018. Carlin-type Gold Deposits in the Dian-Qian-Gui "Golden Triangle" of Southwest China. In: Muntean, J.L. (Ed.), Reviews in Economic Geology-Diversity in Carlin-style gold deposits, 20. Society of Economic Geologists, Inc. Rev. Econ. Geol: Diversity of Carlin-type gold deposits, pp. 157–185.

Su, W.C., Heinrich, C.A., Pettke, T., Zhang, X.C., Hu, R.Z., Xia, B., 2009a. Sediment hosted gold deposits in Guizhou, China: products of wall-rock sulfidation by deep crustal fluids. Econ. Geol. 104, 73–93.

Su, W.C., Hu, R.Z., Xia, B., Xia, Y., Liu, Y.P., 2009b. Calcite Sm-Nd isochron age of the Shuiyindong Carlin-type gold deposit, Guizhou, China. Chem. Geol. 258, 269–274.

Su, W.C., Xia, B., Zhang, H.T., Zhang, X.C., Hu, R.Z., 2008. Visible gold in arsenian pyrite at the Shuiyindong Carlin-type gold deposit, Guizhou, China: implications for the environment and processes of ore formation. Ore Geol. Rev. 33, 667–679.

Su, W.C., Zhang, H.T., Hu, R.Z., Ge, X., Xia, B., Chen, Y.Y., Zhu, C., 2012. Mineralogy and geochemistry of gold-bearing arsenian pyrite from the Shuiyindong Carlin-type gold deposit, Guizhou, China: implications for gold depositional processes. Miner. Deposita 47, 653–662.

Tan, Q.P., Xia, Y., Xie, Z.J., Yan, J., Wei, D.T., 2015. S, C, O, H, and Pb isotopic studies for the Shuiyindong Carlin-type gold deposit, Southwest Guizhou, China: constraints for ore genesis. Chin. J. Geochem. 93, 525–539.

Tomkins, A.G., Pattison, D.R.M., Zaleski, E., 2004. The hemlo gold deposit, ontario: an example of melting and mobilization of a precious metal-sulfosalt assemblage during amphibolite facies metamorphism and deformation. Econ. Geol. 99, 1063–1084.

Wang, L., Long, C.L., Liu, Y., 2015. Discussion on concealed rock mass delineation and gold source in southwestern Guizhou. Geoscience 29, 703–712 (in Chinese with English abstract).

Wang, L., Zhang, Y.W., Liu, S.G., 2009. The application of regional gravity and magnetic data to delineating intrusive bodies and local geological structures in Guizhou Province. Geophys. Geochim. Explor. 33, 246–249 (in Chinese with English abstract).

Wang, Q.F., Groves, D., 2018. Carlin-style gold deposits, Youjiang Basin, China: tectono-thermal and structural analogues of the Carlin-type gold deposits, Nevada, USA. Miner. Deposita 53, 909–918.

Wang, Z.P., 2013. Genesis and Dynamic Mechanism of the Epithermal Ore Deposits, SW Guizhou, China. A Case Study of Gold and Antimony Deposits. Ph.D. thesis, Institute of Geochemistry, Chinese Academy of Sciences, Guiyang, pp. 1–150 (in Chinese with English abstract).

Wang, Z.P., Xia, Y., Song, X.Y., Yan, B.W., Tan, Q.P., 2013. Sulfur and lead isotope composition of the Huijiabao Carlin-type Au field and the ore forming material sources in Southwest Guizhou. Bull. China Soc. Mineral Petrol. Geochem. 32, 746–759 (in Chinese with English abstract).

Wang, Z.P., Xia, Y., Song, X.Y., You, B., Zheng, X.H., Wang, X.Y., 2010. The deep source of the minerals in Carlin-type Au deposit in southwest Guizhou Province: evidence from isotope and REE. Miner. Deposits 20, 519–520 (in Chinese with English abstract).

Williams-Jones, A.E., Bowell, R.J., Migdisov, A.A., 2009. Gold in solution. Elements 5, 281–287.

Williams-Jones, A.E., Norman, C., 1997. Controls of mineral paragenesis in the system Fe-Sb-S-O. Econ. Geol. 92, 308–324.

Wu, Y.F., Evans, K., Li, J.W., Fougerouse, D., Large, R.R., Guagliardo, P., 2019. Metal remobilization during ore-fluid perturbation during episodic replacement of auriferous pyrite from an epizonal orogenic gold deposit. Geochem. Cosmochim. Acta 245, 98–117.

Xia, Y., 2005. Characteristics and Model for Shuiyindong Au Deposit in Southwestern Guizhou, China: Ph.D. Thesis, Guiyang, China. Chinese Academy of Sciences, p. 123 (in Chinese with English abstract).

Xie, Z.J., Xia, Y., Cline, J.S., Koenig, A., Wei, D.T., Tan, Q.P., Wang, Z.P., 2018a. Are There Carlin-Type Gold Deposits in China? A Comparison of the Guizhou, China, Deposits with Nevada, USA, Deposits. In: Muntean, J.L. (Ed.), Reviews in Economic Geology-Diversity in Carlin-style gold deposits, 20. Society of Economic Geologists, Inc. Rev. Econ. Geol: Diversity of Carlin-style gold deposits, pp. 187–233.

Xie, Z.J., Xia, Y., Cline, J.S., Pribil, M.J., Koenig, A., Tan, Q.P., Wei, D.T., Wang, Z.P., Yan, J., 2018b. Magmatic origin for sediment-hosted Au deposits, Guizhou Province, China: in situ chemistry and sulfur isotope composition of Pyrites, Shuiyindong and Jinfeng deposits. Econ. Geol. 113, 1627–1652.

Xing, Y., Brugger, J., Tomkins, A., Shvarov, Y., 2019. Arsenic evolution as a tool for understanding formation of pyritic gold ores. Geology 47, 335–338. https://doi.org/10.1130/G45708.1.

Xu, Y.G., He, B., Chung, S.L., Menzies, M.A., Frey, F.A., 2004. Geologic, geochemical, and geophysical consequences of plume involvement in the Emeishan flood-basalt province. Geology 32, 917–920.

Yan, J., Hu, R.Z., Liu, S., Lin, Y.T., Zhang, J.C., Fu, S.L., 2018. NanoSIMS element mapping and sulfur isotope analysis of Au-bearing pyrite from Lannigou Carlin-type Au deposit in SW China: new insights into the origin and evolution of Au-bearing fluids. Ore Geol. Rev. 92, 29–41.

Yang, W., Hu, S., Zhang, J., Hao, J.L., Lin, Y., 2015. NanoSIMS analytical technique and its applications in earth sciences. Sci. China Earth Sci. 58, 1758–1767.

Yuan, H.L., Liu, X., Chen, L., Bao, Z.A., Chen, K.Y., Zong, C.L., Li, X.C., Qiu, W.H., 2018. Simultaneous measurement of sulfur and lead isotopes in sulfides using nanosecond laser ablation coupled with two multi-collector inductively coupled plasma mass spectrometers. J. Asian Earth Sci. 154, 386–396.

Zhang, J.C., Lin, Y.T., Yang, W., Shen, W.J., Hao, J.L., Hu, S., Cao, M.J., 2014. Improved precision and spatial resolution of sulfur isotope analysis using NanoSIMS. J. Anal. At. Spectrom. 29, 1934–1943.

Zhang, X.C., Spiro, B., Halls, C., 2003. Sediment-hosted disseminated gold deposits in Southwest Guizhou, PRC: their geological setting and origin in relation to mineralogical, fluid inclusion, and stable-isotope characteristics. Int. Geol. Rev. 45, 407–470.

Zhang, X.J., Xiao, J.F., 2014. Zircon U-Pb geochronology, Hf isotope and geochemistry study of the Late Permian diabases in the northwest Guangxi autonomous region. Bull. China Soc. Mineral Petrol. Geochem. 33, 163–176 (in Chinese with English abstract).

Zhang, Y., Yan, D.P., Zhao, F., Li, X.T., Qiu, L., Zhang, Y.X., 2016. Stratigraphic sequences, abundance anomalies and occurrences of as, Sb, Au, Ag in the lower cambrian Niutitang formation in kaiyang phosphate mine area. Acta Petrol. Sin. 32, 3252–3268 (in Chinese with English abstract).

Zhao, J., Liang, J.L., Long, X.P., Li, J., Xiang, Q.R., Zhang, J.C., Hao, J.L., 2018. Genesis and evolution of framboidal pyrite and its implications for the ore-forming process of Carlin-style gold deposits, southwestern China. Ore Geol. Rev. 102, 426–436.

Zheng, L.L., Yang, R.D., Gao, J.B., Chen, J., Liu, J.Z., Li, D.P., 2019. Quartz Rb-Sr isochron ages of two type orebodies from the Nibao carlin-type gold deposit, Guizhou, China. Minerals 399, 2–15.

Zhu, J., Zhang, Z.C., Santosh, M., Jin, Z.L., 2020. Carlin-style gold province linked to the extinct Emeishan plume. Earth Planet Sci. Lett. 530, 115940. https://doi.org/10.1016/j.epsl.2019.115940.

Zhu, J.J., Hu, R.Z., Richards, J.P., Bi, X.W., Stern, R., Lu, G., 2017. No genetic link between Late Cretaceous felsic dikes and Carlin-type Au deposits in the Youjiang basin, Southwest China. Ore Geol. Rev. 84, 328–337.

Zhu, J.J., Zhong, H., Xie, G.Q., Zhao, C.H., Xu, L.L., Lu, G., 2016. Origin and geological implication of the inherited zircon from felsic dikes, Youjiang Basin, China. Acta Petrol. Sin. 32, 3269–3280 (in Chinese with English abstract).